Unpredictable geometry and depositional stacking patterns of mass-transport complexes in salt minibasins

Cerys A. Biancardi[1], Tiago M. Alves[1], Marco Antonio Caçador Martins-Ferreira[2]

[1]3D Seismic Lab, School of Earth and Ocean Sciences, Cardiff University, Main Building, Park Place, Cardiff CF10 3AT, United Kingdom.

[2]Faculdade de Ciências e Tecnologia, Universidade Federal de Goiás, Conde dos Arcos, 74968755 Aparecida de Goiânia, GO, Brazil

Abstract

Mass-transport complexes in a salt minibasin of the Espírito Santo Basin (SE Brazil) are investigated using a high-quality 3D seismic volume and borehole data. A series of six (6), stacked MTCs were identified from the sea floor down to an approximate depth of 1.5 kilometres. These MTCs exhibit a high variability in size and internal structures. Three of the MTCs contain single, discrete landslide deposits while the other three MTCs contain multiple, contemporaneous landslides that merge to span the entire salt minibasin. The data in this work show that Area/Length relationships and the number of contemporaneous landslide deposits within an MTC are random, revealing no obvious relationship with relative location or depth. As such, there are no clear stacking patterns for the MTCs in this minibasin. This implies that landslide deposits can be encountered anywhere within a salt minibasin and, furthermore, the extent of the slope failure and its internal structure are unpredictable. This work concludes that slope instability can be the dominant process of sediment filling Miocene salt minibasins on the continental slope of Espírito Santo. Moreover, there is a strong link between halokinesis and the triggering of landslides in the salt minibasins, but the identification of MTCs

becomes challenging with increasing depth and there is the potential for them to be misrepresented. The identification of basal ramps therefore becomes critical in any analysis; except for the youngest MTC 1, all other complexes show clear basal ramps, and for one of the MTCs the basal ramp is its sole identifying character.

Keywords: South Atlantic Ocean; SE Brazil; geomorphology; mass-transport complexes; salt minibasins.

1 Introduction

Submarine landslides are common features on continental slopes, forming where the downslope driving stress (gravity) exceeds the resisting strength of the sediment (Hampton *et al*., 1996). The rapid accumulation of sediment, local and far-field earthquakes, tectonic oversteepening of the sea floor, and excess pore fluid pressure, all contribute to triggering submarine landslides and associated sediment gravity flows (Locat *et al*., 2002). Resulting strata, commonly named mass-transport deposits (MTDs), are thus found in fjords, active deltas, submarine canyon-fan systems, oceanic-volcanic islands and near salt diapirs (Hampton *et al*., 1996). In these latter structures, halokinesis steepens the flanks of salt minibasin walls to generate local tectonic activity and fractures, all of which combine to make them a prime area for slope instability (Hampton *et al*., 1996; Doughty-Jones *et al*., 2019; Gamboa *et al*., 2019).

Differences between subaerial and submarine landslides are well documented in the literature. In particular, the ratio between headwall length and runout distance is markedly different between submarine and subaerial landslides; hydroplaning at the base of submarine landslides possibly causing an increase in their runout length in the submarine realm (McAdoo *et al*., 2000). One of the largest subaerial landslides ever recorded is the debris avalanche adjacent to Mount Shasta (California), which covers an area of approximately 450 km^2 for a maximum length of 43 km and an estimated volume of 26 km^3 (Crandell *et al*., 1984; Schuster and Highland, 2001). When compared

47 to subaerial landslides, submarine MTDs can be several orders of magnitude larger than subaerial
48 landslides, as in the case of the Storegga Slide (offshore Norway), which affected an area of
49 approximately 95,000 km^2 and displaced a mass of sediment with a volume of 2400 km^3 to 3200 km^3
50 (Haflidason et al., 2005). Large, recurrent landslides are also known offshore the Bay of Bengal and
51 the Grand Banks (Newfoundland), and have recorded the rapid transport of dense gravity flows
52 through vast areas of the continental slope (Calvès *et al*., 2015; Schulten *et al*., 2019; Yamamoto *et*
53 *al*., 2019).

54 The widespread use of sidescan-sonar and 2D seismic data has driven the compilation of large
55 databases of MTDs around the world. The COSTA project (Continental Slope Stability project,
56 spanning April 2000 to March 2004) measured submarine landslides across Europe to find that the
57 largest slides lie on open continental slopes, while the smallest slides are in semi-enclosed basins with
58 restricted sediment flow (Canals et al., 2004). A morphological analysis of slope failure around the
59 US continental slope using GLORIA (Geological Long Range Inclined Asdic) revealed that the
60 largest percentage of surface area affected by slope instability occurs in the Gulf of Mexico,
61 specifically in the region adjacent to the Mississippi Canyon, with landslides within salt minibasins
62 being the smallest (McAdoo *et al*., 2000). Moscardelli and Wood (2016) compiled a database of 332
63 MTDs from a wide range of geological settings. Their results show a relationship between geological
64 setting and the geometry of MTDs, with the latter deposits falling into two categories: *attached* (being
65 proximal to the shelf and upper slope) and *detached* (distal from the shelf and associated with
66 localised slope failure), with the former being the larger (MTD area being greater than 100 km^2). The
67 authors also found a high correlation between length and area of MTDs. A study of MTDs in the
68 Rockall trough (west of Ireland the UK) also related MTD geometry to slope morphology and
69 sediment supply (Georgiopoulou et al., 2014). The relationship between length and area of an MTD
70 was also identified by Katz *et al*, (2015) in an analysis of over 400 MTDs on the continental slope of
71 Israel, with MTD deposits comprising 20%of the studied continental slope. On the convergent

continental margin setting of offshore Chile, approximately 5.7% of the studied slope was affected by MTDs (Völker et al., 2012), with the observed MTDs falling into four categories (canyon wall, open slope, lower slope and superscale slides), each controlled by different failure mechanisms.

Newer classifications of mass-wasting deposits have focused on the characterisation of their source areas and resulting gravity-driven deposits (Mulder et al.,1996; Moscardelli *et al*., 2008), their detailed morphology on near-seafloor data (Frey-Martínez *et al*, 2006; Baeten *et al*., 2013), or on the seismic-morphological dimensions of failed strata and adjacent slope deposits (Alves *et al*., 2010; Clare *et al*., 2018; Ward *et al*., 2018; Gamboa *et al*., 2019). Nevertheless, when compared to open continental slopes, little is known about MTD morphology or predictability in offshore salt minibasins, (Beaubouef and Abreu, 2010; Jackson, 2012; Gamboa and Alves, 2016; Wu *et al.*, 2020), in part due to the inherent resolution limits of sidescan imagery of the sea floor (Johnson *et al*., 1990). There are also few studies on MTDs in salt minibasins that use modern seismic data. Gamboa *et al*. (2010) used 3D seismic data to interpret a sequence of stacked MTDs offshore Espírito Santo Basin, SE Brazil. They have recognised a dominant source direction from the north and northwest, reflecting a non-uniform distribution of MTDs controlled by slope topography and adjacent salt structures. This fits well with the findings of Tripsanas *et al*. (2004), which identified salt-structures controlling MTD distribution. Gamboa *et al*. (2016) also interpreted a bi-modal geometry of MTDs within a salt-withdrawal minibasin, based on the ratio of headwall length to downslope length, concluding that salt structures are not a unique control on MTD geometry; basin confinement should also be taken in consideration. Mass-transport deposits in salt minibasins are thus underrepresented in the literature, and yet they have a significant impact on hydrocarbon exploration. Depending on sediment supply, MTDs can form extensive reservoirs (Shanmugam *et al*., 2009), act as competent seal intervals (Moscardelli, 2006) or, in some instances both supplement and erode reservoir leading to compartmentalisation (Cardona et al., 2016; Henry et al., 2018).

Differentiating between MTDs (mass-transport deposits) and MTCs (mass-transport complexes) is not straightforward when interpreting subsurface structures in seismic data. Pickering *et al*. (1986) recommend the term MTD to be used wherever a single landslide event is apparent, while multiple, stacked mass-wasting deposits should be named as part of an MTC. However, the term MTC is also used in the published literature to name the deposits formed by a succession of related gravity-driven processes such as slides, slumps, debris flows and turbidity currents, in which the vertical stacking of multiple flow events may not have occurred (Pickering *et al*., 2005). This work identifies discrete MTDs and multiple, contemporaneous MTCs, all of which are stacked in a thick succession of Cenozoic strata. For simplicity, the definition of Weimer *et al*. (2004) is applied, with all mass-wasting deposits being called MTCs in this work.

The aim of this paper is to describe MTCs deposited within a salt-withdrawal minibasin in the Espírito Santo basin, SE Brazil, based on their relative location, geometry, transport direction and inferred source areas (Fig. 1). We aim to address the geometrical and temporal relationships between the MTCs and surrounding salt diapirs. As such, this work will focus on the following research questions:

- What is the geometry and distribution of discrete landslide deposits within a stacked mass-transport complex in a salt minibasin?
- Is it possible to predict the stacking pattern of MTCs in salt minibasins based only on seismic data?
- Do MTCs record the discrete periods of halokinesis within a salt minibasin, thereby acting as a chronological proxy for salt-structure growth?

This work studies the evolution of a salt minibasin from the Miocene to Holocene in terms of MTC infill direction and remobilisation. We have analysed strata filling the salt minibasin of interest, approaching ~ 1.5 km in thickness, the majority of which comprises mass-transport deposits (Figs. 1 and 2).

2 Data and Methods

This work uses a full-stack 3D seismic volume covering an area of 1670 km^2 in the Espírito Santo Basin, SE Brazil (Fig. 1). Water depth ranges from 100 m to 1800 m, and the seismic data was acquired with 12.5 m × 12.5 m grid spacing using a 6×5.700 m array of streamers. The acquired 3D seismic volume was prestack time-migrated following the Kirchhoff method. A TAU-P linear noise attenuation and domain deconvolution preceded data processing. Data was acquired with a 2 ms sample rate and resampled to 4 ms with an anti-aliasing filter, being zero-phased with SEG polarity. An increase in impedance is represented by a black peak.

A regional map of the Top Salt reflection was interpreted in detail and used to define the boundaries of the salt minibasin considered in this study. The minibasin of interest is surrounded by salt structures and is roughly spherical with a diameter of ~8 km. Within this salt minibasin, six (6) stacked MTCs were interpreted and labelled MTC 1 to MTC 6. The youngest MTC 1 was interpreted using a single horizon picked on a seismic reflector; the other MTCs are thicker and were constrained by identifying upper and lower horizons that represent the envelope of deformation. Where multiple slope failures are present, and recognised within a single MTC, they are labelled i, ii, iii and so on.

Seismic isochron and attribute maps were used to image the interpreted MTCs with attribute extractions made on their boundary horizons, and RMS (Root-Mean Square) calculations for the seismic interval between the horizons bounding an MTC. Computed maps include: a) *isochron thickness maps*, representing the two-way time thickness in milliseconds (ms TWT) between the upper and lower horizons defining an MTC; b) *variance time-slices and maps*, a measurement of the continuity of the seismic data, scaled 0 to 1 with 0 being maximum similarity (Van Bemmel *et al*., 2000); c) *amplitude maps* showing the amplitude of a seismic reflector as being proportional to the acoustic impedance (or hardness) contrast of the boundary that generated it. Combining these attribute

extractions to create a merged attribute map enhances the imaging of the MTCs interpreted in this study.

Three wells lie immediately to the north and east of the seismic volume and have been used in conjunction with the literature to provide a regional stratigraphic model (Fig. 1). Furthermore, detailed measurements were taken for each discrete landslide within each MTC; area (km^2), length of visible runout distance from head to toe (km) (L in Fig. 3) and flow direction measured as degrees from north (Fig. 3). For MTCs 1, 3 and 5, these measurements represent the absolute length and area of discrete landslides (L in Fig. 3). In turn, MTCs 2, 4 and 6 contain multiple landslides that merged to span the salt minibasin. For these landslides, minimum measurements were taken using the confined zone defined by their basal ramps (Lc in Fig. 3). The maximum lengths and areas are the width and area of the minibasin itself. The lack of imaged headwall scarps in the interpreted MTCs, combined with their chaotic, seismically-opaque internal structures, made the application of Frey-Martínez *et al*. (2006) classification, which describes MTCs as being frontally confined or emergent, relatively easier to apply in the study area than other common classifications. *Frontally confined* is defined as having a compressional toe that is buttressed by a ramp; *frontally emergent* is defined as having compressional toe regions that have overridden ramps, overthrusting downslope undisturbed strata (Frey-Martínez *et al*, 2006). Using this classification system, all the MTCs found in the study are defined as *frontally emergent* and, except for MTC 1, all have basal ramps over which the landslides have emerged (Fig. 3).

3 Geological Setting

The Espírito Santo Basin is located in SE Brazil and covers an area of approximately 125,000 km^2, with 107,000 km^2 lying offshore (Fiduk et al., 2004). The basin is bounded to the north by the Abrolhos Bank, a magmatic plateau dated 40-50 Ma (Chang *et al*., 1992), and to the south by the Campos Basin and the Alto de Vitória (França et al., 2007) (Fig. 1).

The opening of the South Atlantic was initiated on the Gondwana supercontinent during the Late Mesozoic, culminating in the separation of what is currently known as the South American and African plates (Fig. 2). From the Jurassic to the Early Cretaceous, lithospheric extension generated six rift basins along the eastern margin of present-day Brazil (Chang *et al*., 1992), which are together known as the East Brazil Rift System (EBRIS). Rifting progressed from south to north, forming the Pelotas, Santos, Campos, Espírito Santo (the study area) and Jequitinhonha basins. The evolution of these rift basins is divided into four phases: Pre-rift, Syn-rift, Transitional and Drift (Ponte *et al*., 1978; Ojeda, 1982; Chang *et al*., 1992). The four tectonic phases generated four stratigraphic megasequences: pre-rift continental, syn-rift fluvial clastic, transitional evaporitic, and a drift megasequence comprising marine-transgressive and regressive sequences of a smaller order (Fiduk et al., 2004) (Fig. 2).

Continental rifting started in the Early Cretaceous (Valanginian) in association with the magmatism in the Serra Geral (Gibbs *et al*., 2003; Cainelli *et al*., 1999). The Syn-Rift stage extended from the Berriasian to the Early Aptian, producing narrow, lacustrine basins with flanking fluvio-deltaic sediments (Ojeda, 1982; Chang *et al*., 1992; Gibbs *et al*., 2003). The end of the Syn-Rift stage is marked by a Transitional stage of evaporitic deposition that took place from Early to Late Aptian/Albian (Chang *et al*., 1992). The Transitional stage was dominated by the presence of the Walvis–São Paulo Ridge, at the time linked to the Florianópolis Fracture Zone, forming a bathymetric (and volcanic) high restricting the northward expansion of the new South Atlantic Ocean (Chang *et al.*, 1992). The barrier limited water circulation, generated restrictive saline conditions north of the Pelotas Basin, and culminated in the accumulation of anhydrite and halite in excess of 3000 m in thickness (Chang *et al*., 1992; Mohriak *et al*., 2008; Alves *et al*., 2017). These evaporites were instrumental in shaping the Espírito Santo basin.

By the Late Aptian/Early Albian, the region entered a Drift phase of prolonged subsidence, a phase that has been developing until now (Ojeda, 1982). The Walvis–São Paulo Ridge was breached at this

time and the South Atlantic seaway extended into the basins northwards of the barrier (Chang *et al*., 1992). As a result, evaporite deposition ended and marine conditions were extended across the entire Brazilian rift system (Ponte *et al*., 1978; Ojeda, 1982; Chang *et al*., 1992). The early Drift phase records a marine transgression in the Albian, in which carbonate deposition predominated, with marls and shales deposited in the deeper parts of the basin (Ponte *et al*., 1978; Ojeda, 1982; Chang *et al*., 1992). By the end of the Albian, thermal subsidence and flexural loading led to the drowning of carbonate highs. Late Drift sedimentation started in the Eocene with the deposition of the volcaniclastic Abrolhos Formation, and continues to this day (França *et al*., 2007).

Salt structures vary across the Espírito Santo Basin, from salt rollers in its proximal domain, where salt is the thinnest, to salt diapirs and walls in its central part (Fiduk et al., 2004). In the more distal parts of Espírito Santo, salt canopies formed with coalesced tongues and turtle-back structures (Fiduk *et al*., 2004). During the Aptian, tectonic uplift of the Serra do Mar provided clastic sediment to the Espírito Santo Basin, loading SE Brazil's continental margin to trigger the gravitational gliding of salt and widespread halokinesis (Davison, 2007). This halokinesis has been continuous from the Aptian through the Cenozoic, also in response to tectonic uplift and regional tilting resulting from the emplacement of the Abrolhos Bank (Fiduk et al., 2004), a major magmatic plateau that led to the deposition of a large amount of volcaniclastic sediment into the distal part of the Espírito Santo Basin (França *et al*., 2007). The Paleogene uplift of the Serra do Mar, combined with the Abrolhos volcanism and continued halokinesis created large sediment fairways controlling the deposition of turbidite deposits throughout the Paleogene (França *et al*., 2007).

The base of lower Miocene strata is defined by a regional unconformity (França *et al*., 2007). In the Early to Middle Miocene, calcarenites of the Caravelas Formation were deposited in proximal and central parts of the basin, while sandstones of the Rio Doce Formation filled the Rio Doce Canyon system (França et al., 2007). In more distal parts of the basin, where the study area is located, the Urucutuca Formation was deposited as a succession of turbiditic shales, minor sandstones, and marls

in the deepest parts of the basin (França *et al*., 2007). The MTCs in this study were deposited after the Abrolhos volcanism, lying above the lower Miocene unconformity (Fig. 2).

3.1 Local stratigraphy

Wells Guarapari-1, Cajú-1 and Dendê-1 provide important stratigraphic data in the study area, therefore complementing the stratigraphic column of França *et al*. (2007) (Fig. 4). Well Guarapari-1 drilled 1834 m of Miocene and Eocene strata (Urucutuca Formation) consisting of grey, blocky marls interbedded with grey to white calcilutite (Fig. 4). Below the Urucutuca Formation, Guarapari-1 drilled through 2443 m of strata within the Abrolhos Formation, consisting of basalt and thin beds of tuff and volcaniclastic sediments.

Well Cajú-1 found 2669 m of strata in the Urucutuca Formation consisting of thick layers of shales and marls with minor calcilutite, before reaching a thin layer of tuffs of the Abrolhos Formation (Fig. 4). Below the tuffs, the well penetrated 350 m of massive salt (Aptian Mariricu Formation), inferred to be a local diapiric intrusion as below the halite lie Eocene shales and a thicker sequence of Abrolhos Formation volcaniclastics (Fig. 4). These gradually become dominated by shales, before reaching the Cretaceous Urucutuca Formation.

Well Dendê-1 found 1534 m of strata in the Urucutuca Formation, mostly shales with an increasing presence of marl with depth. Below this portion of the Urucutuca Formation, Dendê-1 encountered 150 m of massive halite (Aptian Mariricu Formation), inferred to be diapiric as it lies above Eocene strata in the Urucutuca formation. Below the halite, Dendê-1 penetrated 1531 m of Eocene and Cretaceous strata belonging to the Urucutuca Formation, with the Cretaceous section being dominated by sandstones with minor shales. The absence of the Abrolhos Formation in Dendê-1 is interpreted to result from the well drilling through several faults. However, this cannot be confirmed as the well lies just outside the interpreted seismic survey (Fig. 1).

The three wells confirm França *et al*. (2007) proposition that the Cenozoic Urucutuca Formation is dominated by shales and marls in distal areas of the Espírito Santo Basin, comprising little or no sand, unless transported by canyon systems, of which there is no evidence in the studied minibasin. Although the MTCs interpreted in this work are not penetrated by any wells, they are stratigraphically younger than the regional Abrolhos Formation (H1), and are expected to comprise strata in the Upper Urucutuca Formation, itself dominated by shales and marls, as these lithologies predominate regionally throughout the continental slope of Espírito Santo. The p-wave (Vp) wireline curves in the wells confirm the Abrolhos Formation to be hard in comparison to the softer marls and shales (Fig. 4). Volcaniclastic and interbedded turbidite intervals in the Abrolhos Formation are distinguished by their high-amplitude, internal reflections in seismic data.

4 Seismic stratigraphy of MTCs

The time-structure map of the Regional Top Salt highlights the complex salt structures found in the Espírito Santo Basin, and shows the relative location of the studied salt minibasin (Fig. 5).

The regional seismic line in Fig. 6, crossing the salt minibasin, reveals two diapirs (D1 and D2) bounding it. Horizon H1 is the top of a high-amplitude reflection sequence interpreted as the volcanic Abrolhos Formation, a regional unit also found in wells Cajú-1 and Guarapari-1 to the north (Fig. 3). Below the Abrolhos Formation, horizon H2 marks a regional unconformity that is interpreted as Lower Eocene, i.e. approximately Ypresian in age (Fig. 6). Horizon H3 is interpreted as the Top Cretaceous boundary within the Urucutuca Formation. The MTCs in this study lie within the Miocene to Holocene Urucutuca Formation and are expected to consist of shales and marls. (Fig. 4).

4.1 Structure and distribution of MTCs

A series of six (6), stacked MTCs were interpreted down to a depth of approximately 3.4 s TWT as described in Table 1. These MTCs were labelled from youngest to oldest as MTC 1 to MTC 6 (Fig.

263 7). Measurements of MTC area, length, flow direction and relationship to the diapirs D1-D4 are found
264 in Table 2.

265 *4.1.1 MTC 1*

266 MTC 1 is the youngest in the study area, lying just below the sea floor. On seismic sections, multiple
267 landslides appear as low-amplitude breaks within one positive (black) reflection (Fig. 8). Horizon H1
268 defines the MTC (it is too thin to be defined by two horizons) and is interpreted on a peak. Figure 8
269 shows a variance map of horizon H1 within which six (6) discrete landslides are visible and labelled
270 as i, ii, iii, iv, v, vi. The landslide edges are defined by high-variance values, with chaotic high-
271 variance infill. Headwall scarps are not visible, the travel direction is inferred from the geometry of
272 the landslide deposits; i and ii are sourced from the northwest, four (4) other landslides are sourced
273 from the east and northeast (Fig. 8). Discrete landslides exhibit a range of geometries, their
274 Width/Length (runout length) ratios being bi-modal with ii and iv approximately as wide as they are
275 long, and i, iii, iv and vi having low W/L ratios being longer than they are wide. Comparable
276 measurements of width are not included, as headscarps are not imaged and width varies with runout
277 length. The same variance map in Fig. 8 gives an indication of internal structure, landslides ii, iv, v
278 and vi having highly chaotic, high variance infill. In contrast, landslide i has low-variance infill and
279 landslide iii shows high-variance in its toe zone.

280 *4.1.2 MTC 2*

281 MTC 2 is bounded by horizons H2a and H2b (Fig. 9). This MTC is interpreted to contain multiple
282 landslide deposits that merged to span the salt minibasin. Its internal structure is highly chaotic but
283 with clear basal ramps as imaged in Fig. 9. In the central part of the basin there is a flat (or platform)
284 of undeformed, in-situ strata with high-amplitude reflections parallel to the underlying strata (Fig. 9).
285 This flat is ~ 900 m wide at its narrowest point which is in the section shown in Fig.9 and widens to
286 ~ 2300 m in the centre of the basin. Discrete landslides thicken against this platform and emerge over

287 it onto the basin floor, as shown by the high-amplitude area highlighted in Fig. 9. This high-amplitude
288 zone is interpreted as a deformed slide-block of older (high amplitude) strata that has been transported
289 over the ramp, emerging onto the flat. The curvature of the ramps is interpreted as a kinematic
290 indicator, orthogonal to the direction of movement of MTCs, which combined with the over-ramp
291 slide block and isochron map were used to interpret two (2) landslides (i and ii) sourced from the
292 southwest and southeast.

293 ### *4.1.3 MTC 3*

294 MTC 3 is bounded by horizons H3a and H3b and contains one single landslide deposit (Fig. 10). This
295 landslide is well defined using a combination of the isochron and variance data extracted from the
296 base horizon H3b, and an average RMS variance extraction between H3a and H3b, as shown in Fig.
297 10. The landslide is sourced from the west and thickens against two basal ramps. These basal ramps
298 are orthogonal to the flow direction, have a vertical displacement of ~ 30m, and define where the
299 landslide incised into older strata. Internal seismic reflections onlap the basal ramps and show it as
300 emerging onto the basin floor (Fig. 10). This emergent section and the toe of the landslide are imaged
301 by an RMS variance extraction between H3a and H3b, with the toe having a high variance fill that
302 contrasts with the continuous reflections of surrounding, undisturbed strata.

303 ### *4.1.4 MTC 4*

304 MTC 4 is bounded by horizons H4a and H4b, (Fig. 11). The interval between H4a and H4b is
305 seismically transparent, with almost no reflectivity, as shown by the seismic sections and RMS map
306 in Fig. 11. There are indications of compressional ridges on the variance map. The base of MTC 4
307 contains the only visible structures: two curved basal ramps that span the minibasin, striking
308 approximately north south, and forming the edges of a central flat (or platform) that is ~ 5200 m long
309 (north-south), and ranges from ~ 2000 m to ~ 675 m in width (east-west). The flat exhibits high-
310 amplitude internal reflections that are concordant with the underlying units and is interpreted as

undeformed strata. The insert in Fig. 11 shows a tilted block on the western edge of the flat. This tilted block has not been transported, is approximately 380 m wide (north-south) and 215 m long (west-east). We interpret this feature as recording deformation of the basal ramp, where a small block of the in-situ flat rotated as the MTC flowed up the ramp and emerged onto the flat. The deformation of the basal ramp and flat, combined with the isochron and indications of compressional ridges on the variance map are used to infer the presence of two distinct MTCs. However, the low reflectivity between H4a and H4b is a limitation and there may be alternative interpretations for this structure.

4.1.5 MTC 5

MTC 5 is bounded by horizons H5a and H5b, (Fig. 12) and contains one single landslide deposit, which is also the largest identified in this work with a length of 6.2 km and an area of 15,475 m^2. Its lateral boundaries and toe are well defined in seismic data by using a combination of variance time-slices and isochron maps (Fig. 12). The toe shows a hummocky and chaotic internal structure, with compressional ridges imaged by the isochron map (Fig. 12). Close to the source there is a significant ramp, orthogonal to the flow direction of MTCs, showing a maximum throw of 75 ms (approximately 70 m). This is the largest ramp in the whole salt minibasin. The landslide heavily incised into older strata and thickens significantly to the northeast of the basal ramp (Fig. 12). The lateral edges of the MTC are interpreted on both the isochron map and the variance map, with the internal structure having high variance in comparison to the surrounding strata. The landslide is emergent onto the centre of the basin, and just like MTC 3, is preserved with the toe intact and clearly imaged (Fig. 12).

4.1.6 MTC 6

The lowermost MTC 6 is bounded by H6a and H6b (Fig. 13). The interval has low, internal reflectivity, with chaotic internal structures on the seismic sections. The base (H6b) has multiple, basal ramps that incise into older strata of high-amplitude reflectivity. These basal ramps are highlighted in the variance and isochron maps (Fig. 13) and are interpreted as a series of multi-

directional landslides. The combined attribute map in Figure 13 shows five (5) discrete landslides, defined by basal ramps with thickening of the sediment mass against the ramps. All landslides are emergent in the study area, coalescing to fill the minibasin. The landslides are sourced from a range of directions: southeast, east and northeast. Two of the landslides (labelled iii and iv in Fig. 13) overlap and are interpreted as being regressive landslides. Due to the poor seismic reflectivity, there is a possibility of alternative interpretations of the number of MTCs.

5 Morphometric analysis of MTCs

Table 2 contains a detailed breakdown of the discrete landslides within each MTC, with measurements for length, area, flow direction and inferred source diapir. For MTCs 1, 3 and 5, each discrete landslide has a discernible toe. MTCs 2, 4 and 6 contain multiple landslides that are amalgamated with no discernible toes. For these, measurements for length and area are based on the detailed mapping of basal ramps and thickness variations on seismic sections and isochron maps (Fig. 3). The landslides range in length from 0.9 km to 6.2 km and 1023 km^2 to 15,475 km^2 in area. A high positive correlation (0.74) is observed between length and area for all measurements**.** There is no correlation between flow-direction and length/area.

The cross-plot in Figure 14 displays the measurements of Length vs. Area found in Table 2. The data in the plot fall into two groups: *emergent* MTCs with defined toes (Fig. 15a and 15b), and *confined* MTCs that are merged with no visible toes (Fig. 15c). For all the MTCs, the most frequently found are small in area and length.

The main finding of this paper is that MTCs are ubiquitous in the interpreted minibasin and comprise one of the main processes of sediment transport into salt-rich basins, which is consistent with previous studies (Beaubouef and Abreu, 2010; Wu et al., 2020) (Fig. 15). Nevertheless, the six (6) MTCs mapped in this work display a wide range of geometries and morphologies. Figure 16a shows the six MTCs stacked on top of each other in the minibasin. The basin is surrounded by salt structures and

359 underlain by a salt weld. The evacuation of the salt that led to the salt weld generated continuous
360 accommodation space for sediment. The tectonically active salt structures that surround the minibasin
361 resulted in unstable and continuously steepening basin slopes (Giles and Lawton, 2002; Giles and
362 Rowan, 2012; Mianaekere and Adam, 2020), which combined with a high sediment input into the
363 Espírito Santo basin (Gamboa et al., 2010), triggered recurrent submarine landslides that sourced the
364 MTCs interpreted in this work. Where MTCs have been analysed in salt minibasins, many have been
365 limited by only having near-surface data (bathymetric and side-scan sonar images), as in the case of
366 the Bryant Canyon, Gulf of Mexico (Tripsanas *et al*., 2004). Where 3D seismic has been used, the
367 MTCs analysed are discrete slope failures, e.g. offshore Angola (Lackey *et al*, 2018) and in the Santos
368 Basin (Jackson, 2012). Stacked MTCs in salt minibasins are underrepresented when compared to
369 open-slope continental shelf MTDs; Omosanya *et al*. (2013) focused on the provenance of MTCs,
370 Beaubouef and Abreu, (2010) considered MTD placement implications for hydrocarbon exploration,
371 and Wu *et al.* (2020) ;analysed stacked MTDs in the Gulf of Mexico. Close to the study area, Gamboa
372 *et al*. (2016) studied stacked MTCs, finding a bi-modal deformation styles defined by headwall width
373 / distance-to-toe length ratios, with Type 1 W/L < 1, and Type 2 W/L > 1. This bi-modal morphology
374 is especially clear in the youngest MTC in this study (MTC 1), with two adjacent MTCs (labelled i
375 and ii in Fig. 8) having differing Width/Length ratios.

376 Rafted, or slide blocks are frequently observed within MTCs in salt minibasins, for example offshore
377 Angola (Gee at al., 2006) and within the Espírito Santo Basin (Omosanya and Alves, 2013; Alves,
378 2015; Gamboa and Alves, 2016). However, in this study no well-defined, transported blocks have
379 been found. The lack of slide blocks in the study area might be related to the high sedimentation rates
380 and frequency of slope failure, leading to soft and unlithified sediments being transported in the
381 landslides, not hardened sediment and rock. An alternative hypothesis is slope failures being so
382 destructive that blocks were not preserved. Evidence of this is MTC 4, which contains a tilted block
383 on the edge of the preserved flat, interpreted as deformation of the basal ramp (Fig. 11). The presence

of this tilted block suggests that ripping up and shifting older strata was the process in which the landslide deformed and mobilised pre-existing strata, with the lack of preserved rafts elsewhere in MTC 4 suggesting they were broken up. In parallel, MTC 2 contains a high-amplitude zone adjacent to a basal ramp and, although highly deformed, may have initially been a slide block. As a result of this interpretation, the second main finding of this work includes the realisation that the interpreted MTCs fall into three categories, as summarised in Fig. 15:

1. Type 1, comprising discrete landslide deposits with defined toes but no basal ramps;
2. Type 2, represented by discrete landslide deposits with defined toes and basal ramps;
3. Type 3, comprising multiple, coalesced landslide deposits with different source locations, no toes, and basal ramps. The landslides have merged and span the entire minibasin.

Type 1 is only found in the youngest MTC 1, with Types 2 and 3 alternating with depth in the interpreted salt minibasin (Table 3).

6 Discussion

6.1 A depositional model for MTCs filling salt minibasins

MTC 1 is distinct from the other five MTCs; it is the only MTC without basal ramps and, unlike MTCs 2, 4 and 6, landslides in MTC 1 have defined toes and do not merge. MTC 1 may therefore represent an initial failure state prior to burial and compaction. Alternatively, MTC 1 may be unique due to differences in lithology and slope morphology in comparison to the older MTCs. The latter model seems less likely, as there is no evidence for significant stratigraphic variations between MTC 2 and MTC 1 – the Miocene-Holocene Urucutuca Formation is composed of marls and shales in nearby wells. The presence of MTC 2 directly underneath MTC 1 suggests there were no significant changes in slope gradient or lithology between the two events. We therefore prefer the first explanation above, with MTC 1 representing the early stages of MTC emplacement, before its burial.

MTC 3 contains a single landslide with clear basal ramps (orthogonal to flow), thickening within the confined zone defined by the ramps, and showing a thin over-ramp emergence that forms the defined toe. We propose that MTC 3 represents a landslide preserved at the point of emergence on the basin floor.

MTCs 3 and 5 contain discrete landslide deposits with defined toes and visible internal structures. They both contain basal ramps that are orthogonal (or near-orthogonal) to the landslide flow directions. In the case of MTC 5, its significantly larger ramp and thick confined zone (Lc in Fig.3) may be related to remobilisation triggered by movement of a large fault close to the head of the landslide, which was putatively active until MTC 1 was emplaced (Fig. 12). The size of the ramp and the presence of the fault suggests that frequent slope failure around active faults were able to erode into older strata.

For MTC 4 there is no internal seismic reflectivity, so the curvature of the ramps, combined with the tilted platform block are used as kinematic indicators. This allows us to infer two MTCs sourced from the west-southwest and east-northeast, respectively, as shown by the red arrows in Fig. 11.

Basal ramps form the boundaries of flats (or platforms) of older, in-situ strata in MTCs 2 and 4. In both MTCs, the flats are in the centre of the minibasin. This preservation of pre-existing sediment may be explained by landslides losing energy the farther they travelled down dip. By the time they reached the central part of the basin they were no longer able to rip-up and deform in-situ beds, resulting in the preservation of a central platform, or flat. As basal ramps are related to sediment remobilisation in the study area, we propose a three-phase model of MTC growth:

1. Initial slope failure with no ramping, possible multiple slope failures occur in a similar seismic time scale, e.g. MTC 1. This process produces Type 1 MTCs.
2. Burial, compaction, basin-wall steepening and fault movements trigger the remobilisation of mass-transport deposits. The confined state of the movement leads to deepening of the failure

plane, with older strata being amalgamated into one MTC. Where the failure plane can no longer deform older strata, a ramp forms and the remobilised mass emerges over it. The final emergence over a ramp is onto the basin floor, as shown by MTCs 3 and 5. This process produces Type 2 MTCs.

3. Where multiple slope failures have occurred at similar times, the same processes of burial, compaction, basin-wall steeping and possible fault movements lead to a similar remobilisation as in Phase 2 but, in this particular case, there would be multiple emergences of remobilised masses onto the basin floor that merge. The result is a minibasin-wide amalgamated mass comprising multiple MTCs, for example MTCs 2, 4 and 6. This process produces Type 3 MTCs.

It is important to note that MTCs 4 and 6 are seismically transparent, with no internal reflections. They are distinguished solely by the presence of clear basal ramps on seismic data, but deeper and more deformed MTCs may not have recognisable ramps due to the natural resolution limits of seismic data. This steepening of the basin walls and associated deposits may also lead to basal ramps being misinterpreted as faults. The lack of examples of stacked MTC sequences in salt minibasins may be due to them being under-interpreted in vintage seismic data.

6.2 Do MTCs record distinct pulses of halokinesis, thereby acting as a chronological map of salt-structure growth?

Within the MTCs containing multiple, contemporaneous landslides (MTCs 1, 2, 4 and MTC 6) the question of dating discrete slope instability events is challenging. MTCs 2, 4 and 6 contain multiple slope failures with low to no seismic reflectivity, making the relative dating of slope failures very hard to achieve. MTC 6 is the interval interpreted to contain an apparent retrogressive series of failures (iii and iv in Fig. 13d); therefore, the failure sequence can be estimated as iii then iv, assuming slope failure progresses up dip (Varnes, 1978; Hampton at el., 1996).

MTC 1 is unique in the study area, containing multiple discrete landslides that have not coalesced into one large MTC. Each landslide deposit within the complex is well imaged, including their frontal toe areas. They lie on the same seismic reflector, effectively being contemporaneous (Fig. 8). Hence, is it likely that all six landslides occurred at the same time? One interpretation is that an event occurred that caused widespread slope failure, i.e. an earthquake. An alternative explanation is that a series of halokinetic pulses caused a cascade of slope failures that were not instantaneous but appear so on seismic data.

Although there is a seeming lack of stacking patterns or predictability in the MTCs, a dominant flow direction is evident in seismic data, as shown in Fig. 16b. We interpret this bimodal distribution as being related to the salt structures surrounding the minibasin, and suggest three distinct models for the distribution of MTCs:

A) Salt tectonism is the dominant trigger mechanism for slope failure

B) Salt tectonics and a secondary factor such as regional earthquakes act as triggering mechanisms.

C) Slope failure is random and unrelated to salt movement.

We favour Model A, in which salt movement is the major trigger for slope failure in this minibasin. The analysis in this work shows two dominant source directions, northeast and southwest, shown in the rose diagram in Figure 16b. These bimodal flow directions suggest slope failure was not randomly distributed. These flow-directions directly relate to two diapirs: D2 (east to northeast of the minibasin) and D4 (west to southwest of the minibasin), leading us to conclude that movement on these diapirs caused this bimodal failure distribution. Chronologically, MTCs have been sourced from the northeast and southwest continuously throughout the Miocene to Holocene. It is possible to infer that diapirs D2 and D4 have been active throughout this time (Fig. 16c). Rapid variations in source location between MTCs lends weight to the argument that salt tectonics is the dominant mechanism triggering MTCs. For example, MTCs 1 and 2 have no correlation between flow-direction, with MTC

1 being sourced from diapirs D1 and D2, and MTC 2 by D3 and D4. This almost 180^{o} flip in sources is interpreted as periods of time in which different diapirs were moving, with pulses of salt-tectonic activity triggering slope failure.

It is nevertheless problematic to overlook Model B completely; regional earthquakes may have been the trigger for some of the slope failures. Interpretation and analysis of slope failures at a regional scale would be required to determine if slope failures occurred at the same time, triggered by an earthquake (Assumpção et al., 2011) or major storm (Locat and Lee, 2002), for example – such an analysis is beyond the scope of this work. The repeated, stacked MTCs found in this work suggests it would be unlikely for an external trigger to occur so frequently.

The emplacement of MTCs 1 to 6 is therefore interpreted to be driven by salt tectonics, with pulses of movement in diapirs being the trigger for slope failure. Detailed interpretation of stacked MTCs creates a map of salt-movement over time, in effect slope failures act as proxies for halokinesis. The reverse of this is observation is potentially also true, that if the relative chronology of salt-diapir movement was known, reasonable estimates could be made for flow-direction during MTC emplacement. However, a key unequivocal conclusion of this work is that no clear stacking patterns are observed for the MTCs in the interpreted minibasin. This implies that landslide deposits can be encountered anywhere within a salt minibasin and, furthermore, the extent of slope failures and the internal structure of resultant MTCs are unpredictable.

6 Conclusions

Submarine landslides are known to occur in salt minibasins, with salt diapirism steepening the flanks of the minibasin walls, generating at the same time local tectonic activity and fractures. All these processes contribute to triggering slope failures. Mass-transport complexes (MTCs) in a salt minibasin of the Espírito Santo Basin (SE Brazil) were investigated and recognised as a series of six,

stacked MTCs identified from the sea floor down to an approximate depth of 1.5 kms. The main conclusion from this study are as follows:

a) Slope-failure is the dominant process of Miocene sediment infill within the investigated salt minibasin, offshore SE Brazil;

b) Although ubiquitous, the MTCs in this study exhibit a high variability in number of landslide events within an MTC, its size, location, and internal structure;

c) The MTCs in this minibasin do not exhibit any stacking patterns or predictability in terms of their distribution. Thus, an MTD can be encountered at any depth or location within this minibasin;

d) There is, however, one common denominator for the MTCs, basal ramps are present in all of them, bar the youngest. Basal ramps form where the failure plane can no longer deform older strata, the slip plane becomes discordant with underlying strata and the MTC emerges over the ramp. For one of the interpreted MTCs (MTC 3), the basal ramp is the sole identifying factor;

e) The lack of clear, post-burial seismic markers for MTCs means that the identification of MTCs becomes increasingly challenging with depth. As a result, MTCs may be misinterpreted in similar basins.

In essence, no clear stacking patterns are observed for the MTCs in the salt minibasin investigated in this work. This implies that landslide deposits can be encountered anywhere within a salt minibasin and their internal structure is unpredictable. However, despite their unpredictability there is a strong link between halokinesis and the triggering of landslides in the study area and we propose that mapped MTCs can be used as a proxy for characterising, and dating, salt tectonism.

Figure Captions

Figure 1. (a) Map of South America and Brazil showing the relative location of the study area in the inset map. b) Location of the Espírito Santo Basin and the study area, showing bathymetric contours

at 1000 m intervals. AS: Almirante Saldanha seamount; CF: Cabo Frío Arc; FFZ: Florianópolis Fracture Zone; RJFZ: Rio de Janeiro Fault Zone, RC: Royal Charlotte seamount. (c) Variance time-slice at 3.6 s showing the location of the three wells Guarapari-1, Cajú-1 and Dendé-1 and the salt minibasin analysed in this study.

Figure 2. Stratigraphic column for the Espírito Santo Basin adapted from Mattos *et al*. (2018). Regional horizons and the MTC sequence interpreted in this work are shown in the figure.

Figure 3. Detailed description of the MTC geometrical properties measured in this work. S - zero thickness proximal edge of an MTC, T - toe of a landslide, R - top of ramp defining the end of confined zone, L - length of mass deposit with defined toe, Lc - length of confined zone from S to R. (a) Discrete landslide deposit with defined toe region. (b) MTC containing multiple landslides sourced from different source locations and reflecting distinct flow directions. The landslides have merged to form an MTC that spans the whole of the salt minibasin.

Figure 4. Correlation panel for Wells Dendê-1, Cajú-1 and Guarapari-1 flattened on the Urucutuca Formation D45 well marker. Information displayed in the figure are lithology, Gamma-Ray (GR) and Vp (p-wave) wireline curves.

Figure 5. a) Regional map of the Top Salt horizon in milliseconds two-way time (TWT) showing the locations of exploration wells and the outline of the salt minibasin analysed in this study. b) Regional Top Salt TWT grid, computed with a contour interval of 100 ms. The location of the seismic sections used in this work are shown in the figure. Salt diapirs are labelled D1 to D4.

Figure 6. a) Uninterpreted regional seismic line crossing the studied salt minibasin.

Figure 6. b) Interpreted regional seismic line. Horizon H1 marks the top of the Abrolhos Formation, H2 is an Eocene Unconformity and H3 is the Top Cretaceous. The sea floor down to H1 comprises the upper part of the Urucutuca Formation with marls and shales of Miocene to Holocene age. The

548 Abrolhos Formation, spanning the interval from H1 to H3, comprises volcanic and tuffaceous
549 sediments of Eocene age. The lower part of the Urucutuca Formation is imaged from H3 down to
550 Top Salt. It comprises marls and shales of Cretaceous age. The inset box highlights the area of interest
551 containing the MTCs of Miocene to Holocene age (Fig. 7)

552 **Figure 7. a)** Uninterpreted section of the seismic profile in Figure 6a. **b)** Geological model of the
553 uninterpreted seismic line in a). Horizon H1 is the top of the Abrolhos Formation, H2 is a regional
554 Eocene Unconformity, H3 is the Top Cretaceous. The MTCs interpreted in this minibasin are
555 displayed, from the sea floor down to ~ 3500 s. **c)** Location of the seismic section on a time-structural
556 map of the Top Salt.

557 **Figure 8. a)** Seismic section in the eastern side of the studied minibasin and showing horizon H1 as
558 containing low-amplitude segments interpreted to be MTC 1. **b)** Top Salt TWT grid and variance
559 map extracted from H1. **c)** variance extracted from H1 revealing six landslide deposits, numbered i
560 to v. Red arrow shows the transport direction of discrete landslides.

561 **Figure 9. a)** Section of an east-west seismic profile in the south of the minibasin. The section shows
562 MTC 2 bounded by horizons H2a and H2b. The highlighted area contains a deformed slide block that
563 consists of the same high-amplitude strata as the central flat. This slide block was thrust up the ramp
564 and emerged onto the flat. Two ramps forming the edges of the central flat with the two MTCs
565 emerging over it and merging together. **b)** RMS variance average between H2a and H2b showing the
566 location of section over a Top Salt TWT grid. **c)** Variance map merged with the isochron thickness
567 of MTC 2 (TWT thickness between H1a and H1b). Transport direction is shown by the red arrows.
568 **d)** Merged variance and RMS amplitude maps between horizons H2a and H2b. The high-amplitude
569 over-ramp emergence indicated on the seismic section is highlighted in the figure.

570 **Figure 10**. **a)** Seismic section showing a portion of an east-west profile through the centre of the
571 minibasin. The figure shows MTC 3 to be bounded by horizons H3a and H3b. There are two basal

572 ramps in this region, as highlighted in the section. The inset box shows a zoomed portion of the MTC
573 onlapping the ramp and the undeformed central part of the minibasin where the MTC emerged onto
574 the basin floor. **b)** Isochron map of the succession between horizon H3a and H3b. **c)** Variance map
575 of horizon H3b (base of MTC 3) merged with the isochron map in b). **d)** Variance map between H3a
576 and H3b merged with the isochron map in b). The transport direction of MTD 3 is shown by a red
577 arrow, while its edge is highlighted by a dashed white line.

578 **Figure 11. a)** Seismic section of an east-west profile crossing the centre of the minibasin. The figure
579 shows MTC 4 to be bounded by horizons H4a and H4b. There are two basal ramps that span the
580 minibasin, bounding a central flat of undeformed strata. The inset box highlights this flat, the western
581 side of which is tilted and no longer fully in-situ. **b)** Isochron map of the interval between horizons
582 H4a and H4b. **c)** Variance map of horizon H4b (base of MTC 4) over the isochron map in b). The
583 two basal ramps are labelled A and B. **d)** Variance map of horizon H4b merged with the isochron
584 map shown in b). Two MTCs are interpreted using the basal ramps and thickening of the isochron,
585 labelled i and ii, with inferred transport directions shown by red arrows.

586 **Figure 12**. **a)** Seismic profile oriented SW – NE showing MTC 5 and horizons H5a and H5b bounding
587 it. A large fault cuts across the MTC close to a large basal ramp over which the MTC emerges onto
588 the minibasin floor. **b)** NW-SE seismic section cuts across MTC 5, showing the upper and horizons
589 as being highly rugged. MTC 5 shows discontinuous reflections in its interior. **c)** Isochron map
590 between H5a and H5b) with the edge of the MTC highlighted by a dashed-white line. **d)** Variance
591 map between H5a and H5b. Direction of flow indicated by a red arrow, with the salt diapir D1 being
592 highlighted in the figure.

593 **Figure 13. a)** Seismic section crossing the centre of the minibasin and showing MTC 6 as bounded
594 by horizons H6a and H6b. **b)** Isochron map between H6a and H6b, showing that MTC 5 eroded into
595 MTC 6 – as highlighted by the black polygon. **c)** Variance map of horizon H6b (base of MTC 6),

showing basal ramps, from which the most continuous is Ramp A (also shown on the section). **d)** Variance map of horizon H6b merged with the isochron map in b). Here, multiple landslide deposits are interpreted to have emerged over the ramps to merge together and span the entire minibasin. Five (5) landslide deposits have been interpreted using the attribute maps, and are outlined with dashed-white polygons and labelled i to v, with their transport directions indicated by red arrows. Landslides iii and iv are interpreted as retrogressive, with iv being the youngest.

Figure 14. Cross plot of area vs. length for each discrete MTC interpreted in the study area (see Table 2). The data plotted in the graph falls into two clusters: 1) emergent MTCs with defined toes (MTC1 MTC3 and MTC5) and 2) MTCs with multiple landslides that merged inside the minibasin, so that measurements are taken using the confined zones Lc (Fig.3) defined by basal ramps and isochron maps (MTC2 MTC4 and MTC6). Polynomial trends are shown for each group; emergent and confined.

Figure 15. Types of MTC found interpreted in the study area: a) Type 1: MTC containing discrete landslides with defined toes and no basal ramps. b) Type 2: MTC containing discrete landslides with defined toes and basal ramps. c) Type 3: MTC comprising multiple, coalesced landslides that have merged to span the entire salt minibasin, with basal ramps.

Figure 16. a) Top Salt TWT map with all six MTCs superimposed on one another, coloured by MTC. Individual salt structures are labelled D1 to D4. There is no apparent relationship between the size of an individual landslide deposit, or MTC, and its flow direction. Landslide deposits with different geometries may also have the same sources and flow directions. The stacking pattern of the MTCs illustrates their ubiquitous nature in the studied salt minibasin. b) Flow direction chart for all MTCs, bin size 20^{o}. The two most dominant directions are NE and SW, and are interpreted as resulting from the effect of diapirs D2 and D4 as triggers of most MTCs in the study area. c) Relationship between

diapirs D1 to D4, MTCs 1 to 6, and depth (or age). D2 and D4 are the most active, triggering MTCs nearly continuously throughout this period.

Table Captions

Table 1. List of horizons interpreted and their associated MTCs. Apart from MTC1, each MTC is defined by a clear upper and lower horizon.

Table 2. Analysis of the six MTCs, with measurements for area, length, flow direction and relationship to a diapir. The measurements taken within confined zones (Fig.3b) of interpreted MTCs (using ramps as limits to the MTC) are in grey. The MTCs with defined toes (Fig.3a) are in black. A positive correlation is seen between area and length.

Table 3. Summary of the interpreted MTCs and corresponding classifications based on Figure 16: Type 1 - discrete MTDs without basal ramps. Type 2 - discrete MTDs with basal ramps. Type 3 - multiple, merged MTDs with basal ramps.

Figures

Figure 1

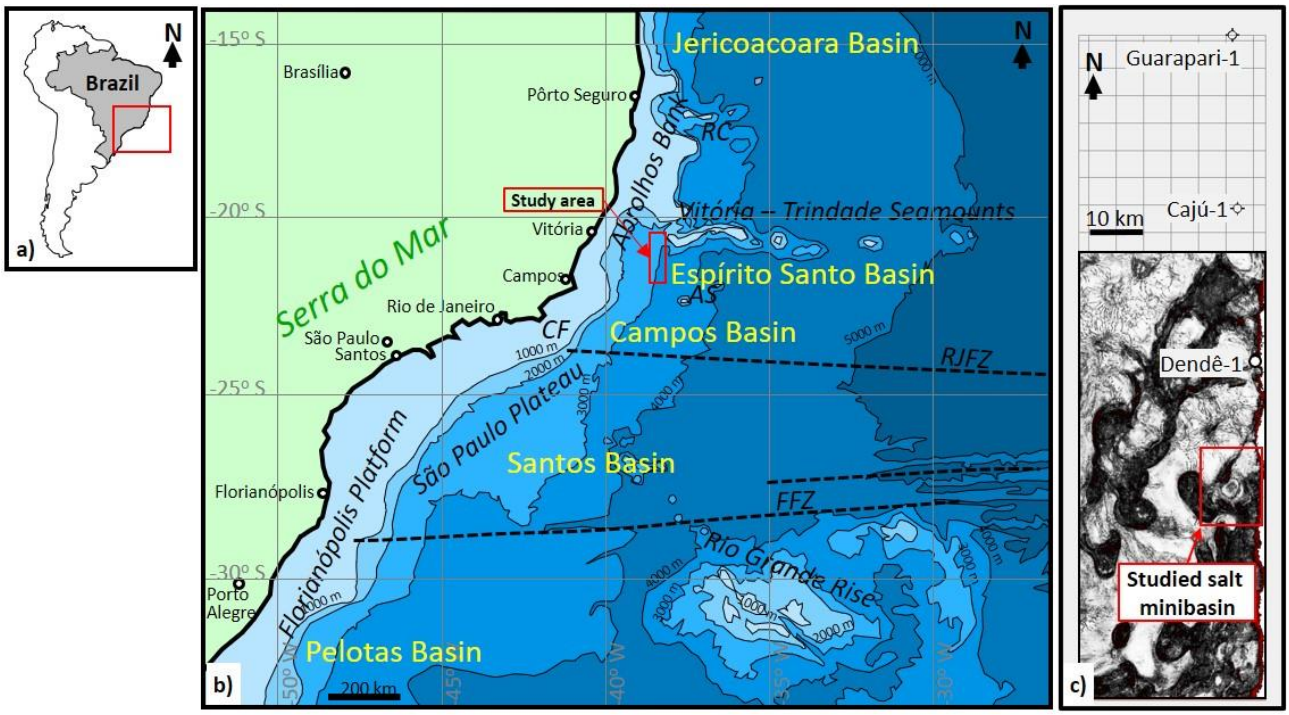

640 Figure 2

641

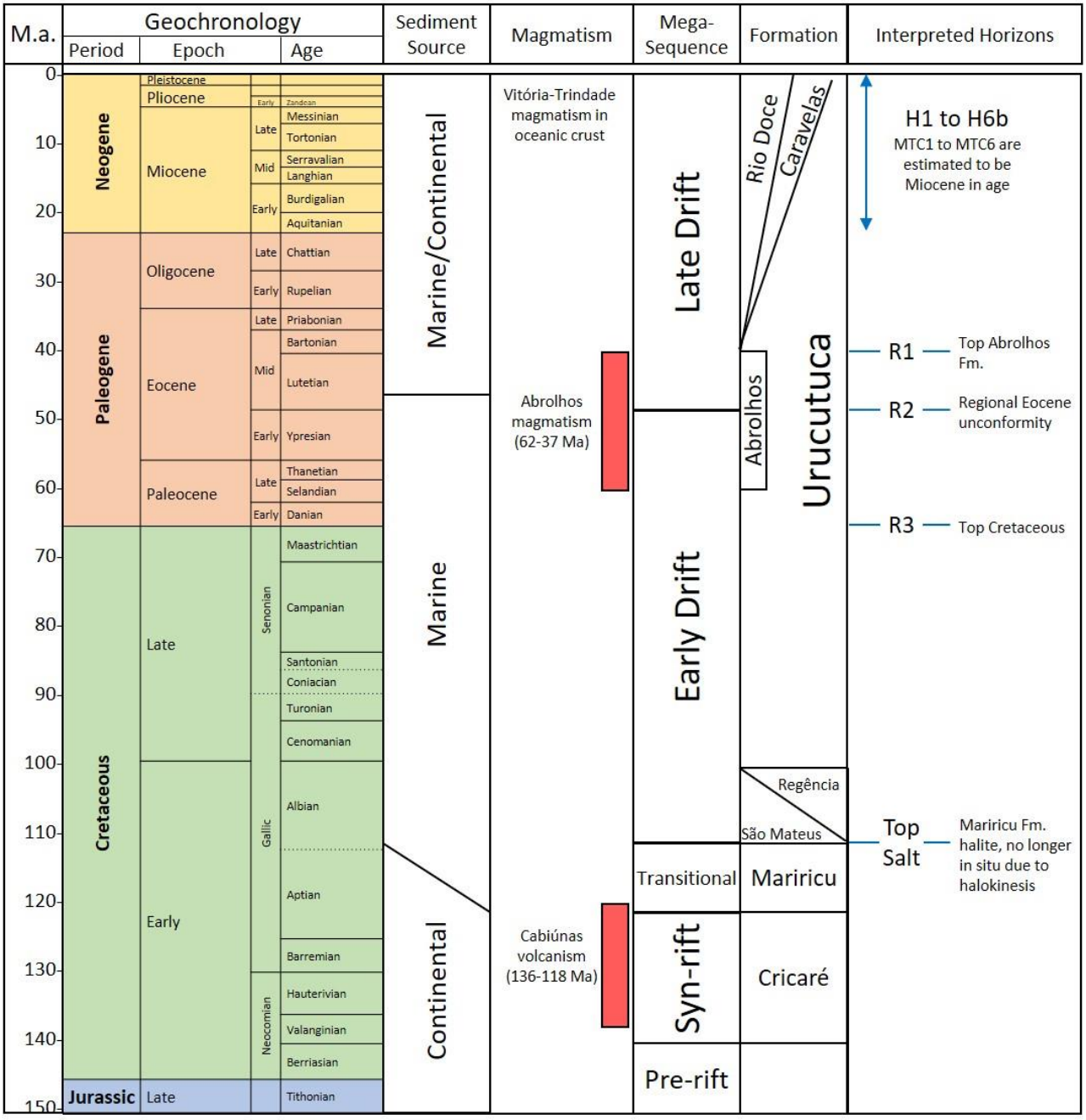

642

643

644 Figure 3

645

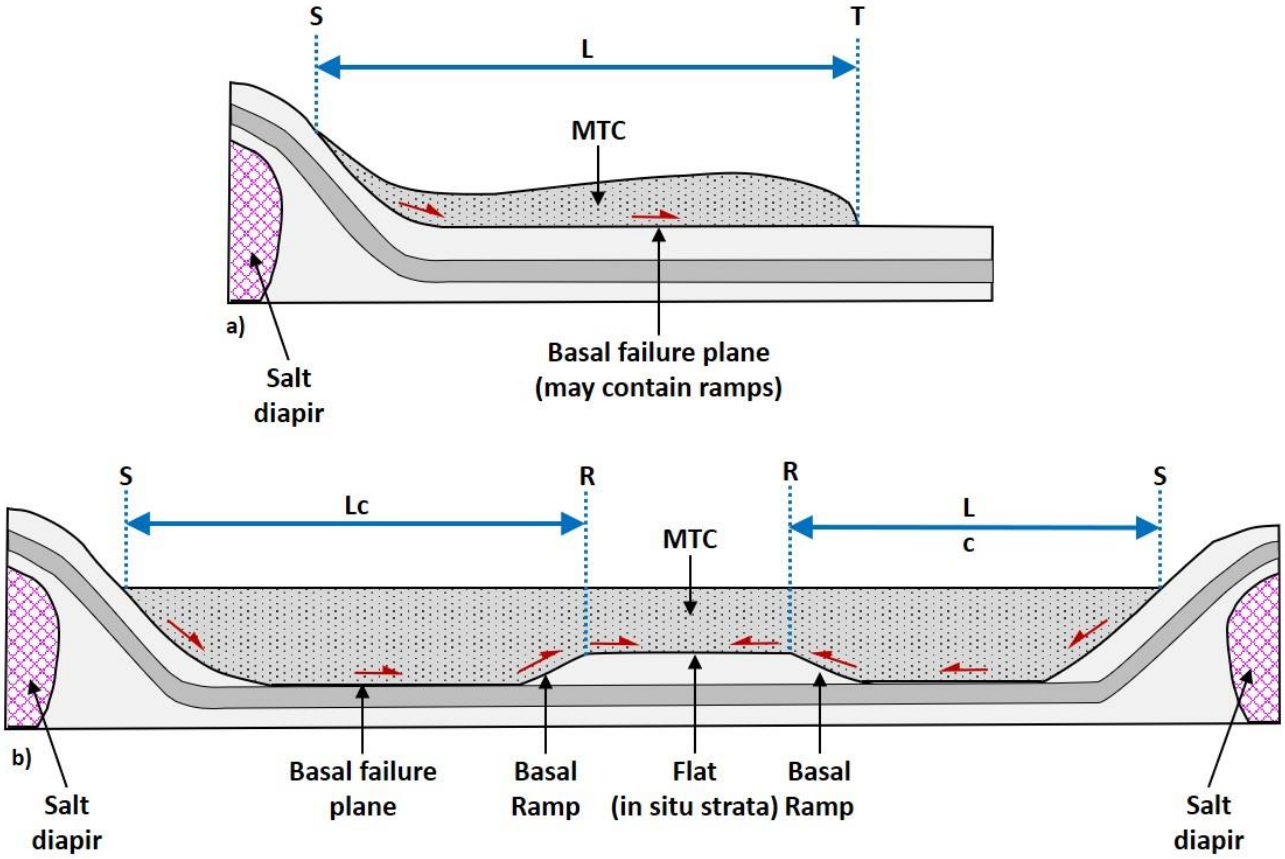

646

647

648 Figure 4

649

650

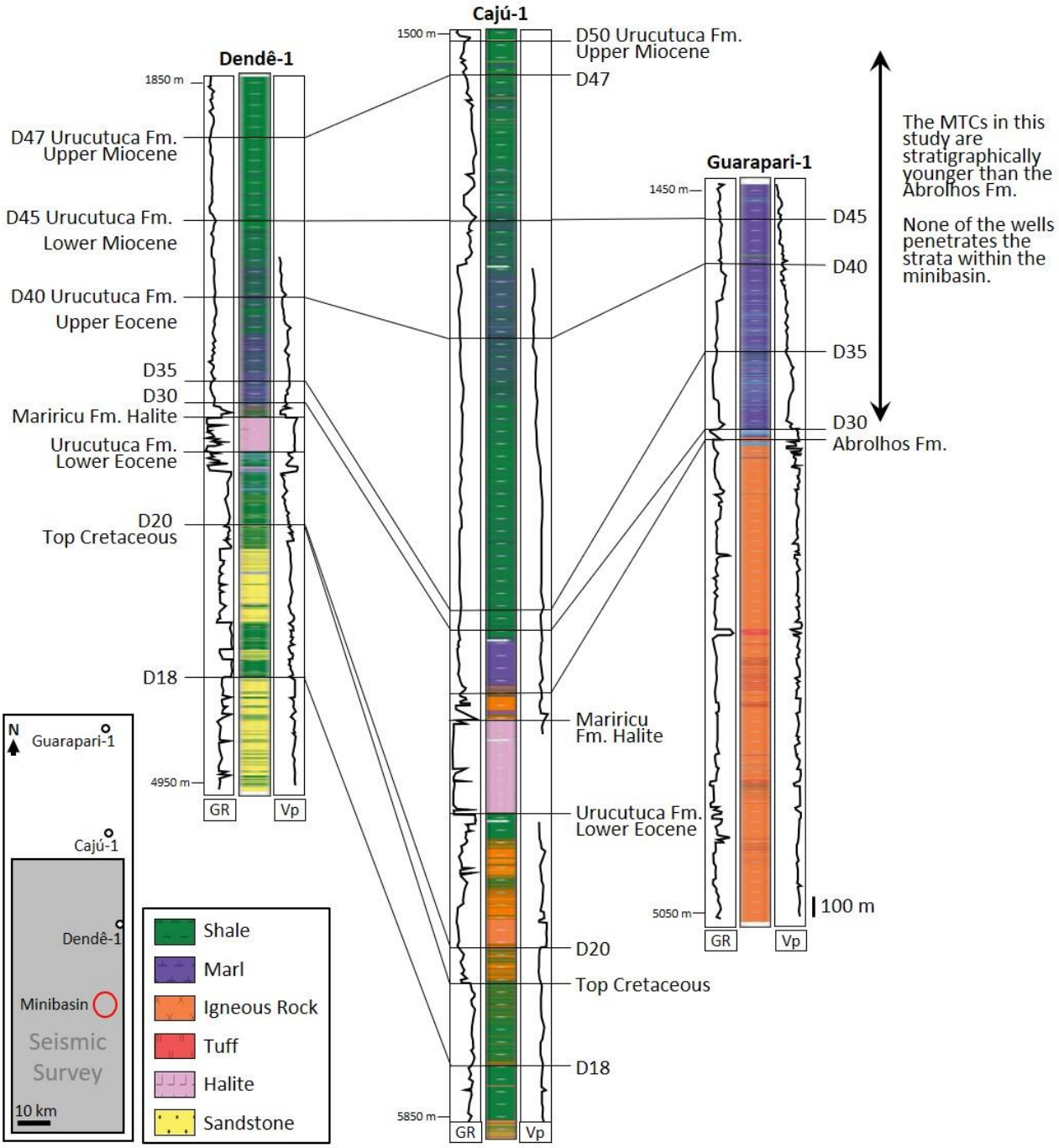

651

652 Figure 5

653

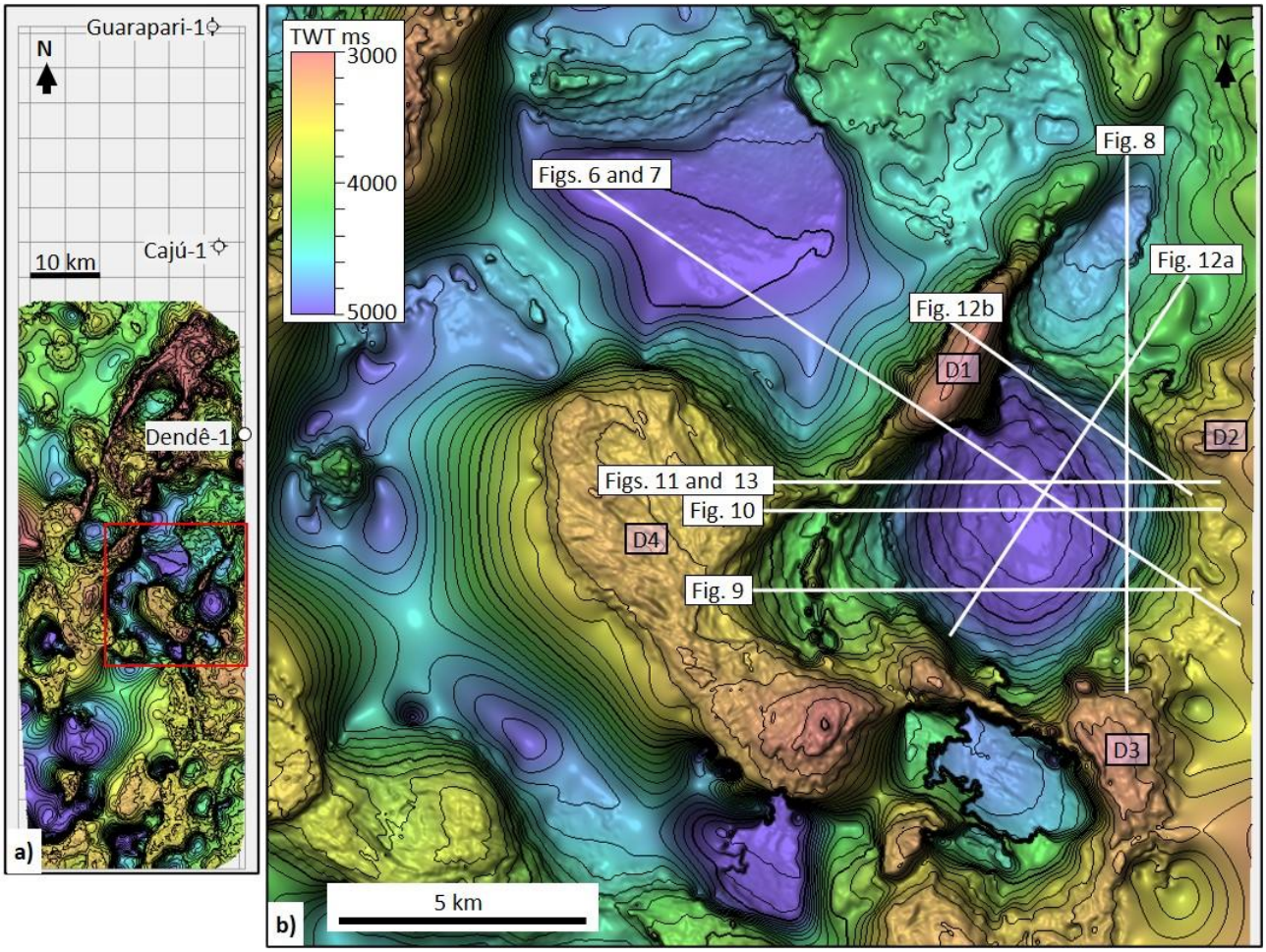

654

655 Figure 6a

656

657

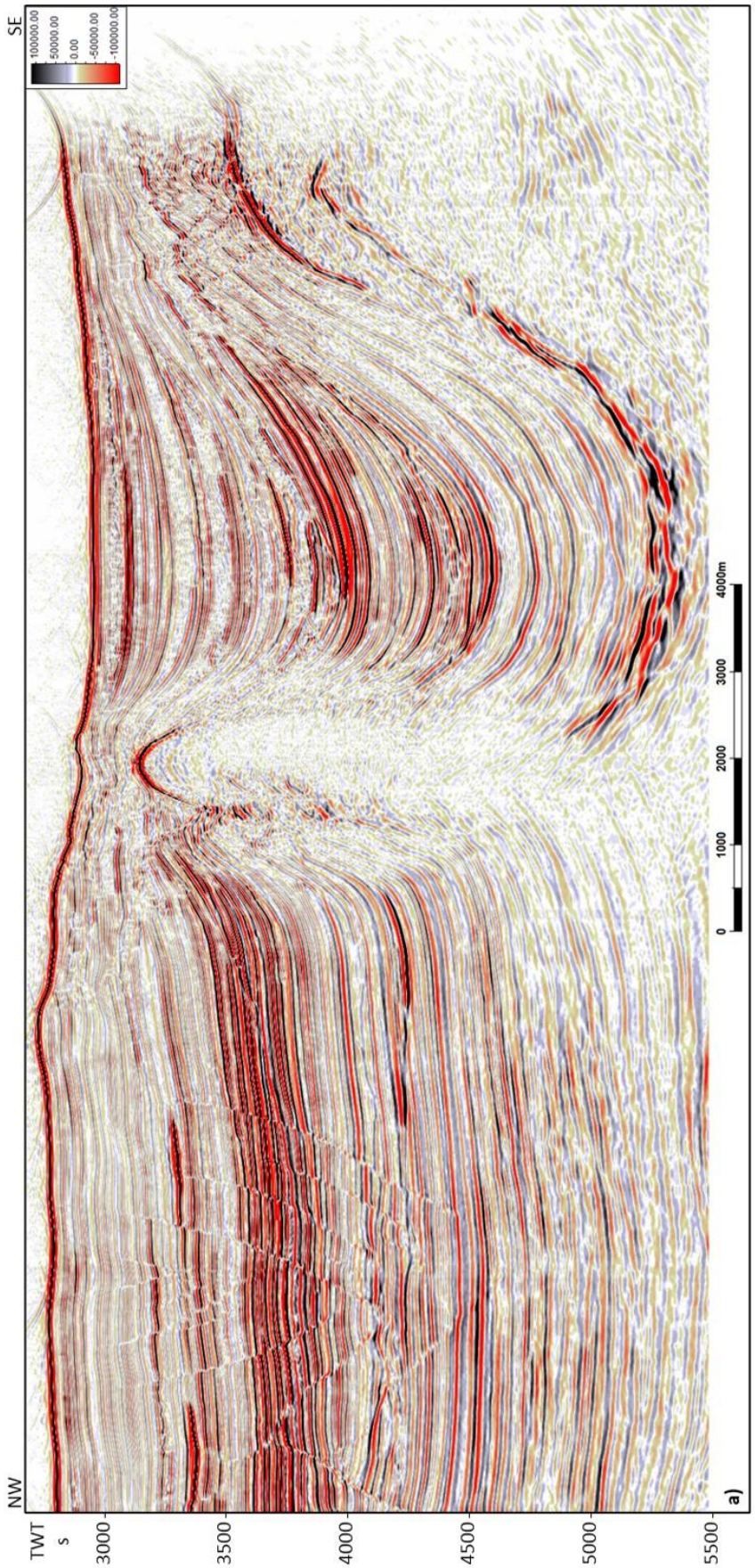

658 Figure 6b

659

660

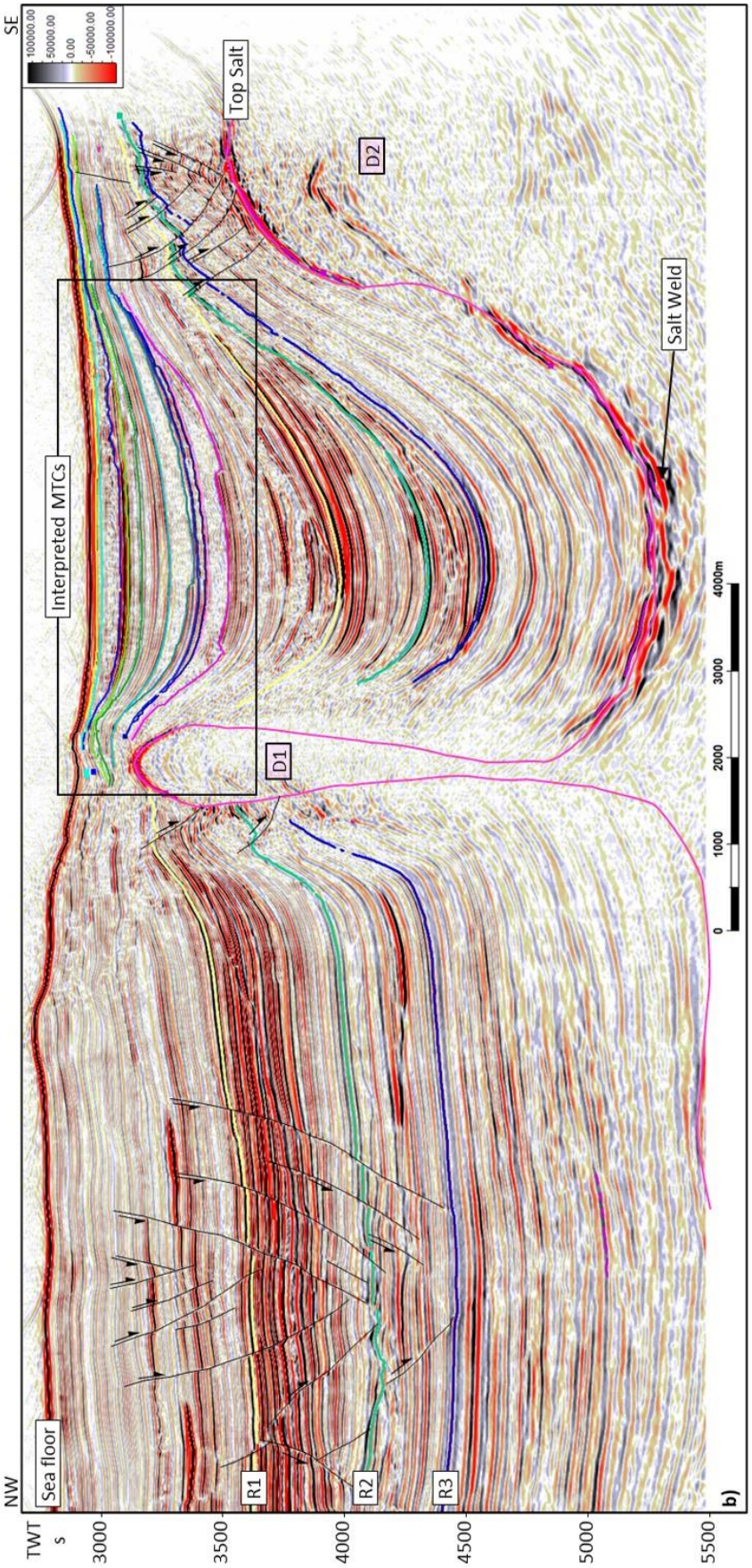

661 Figure 7

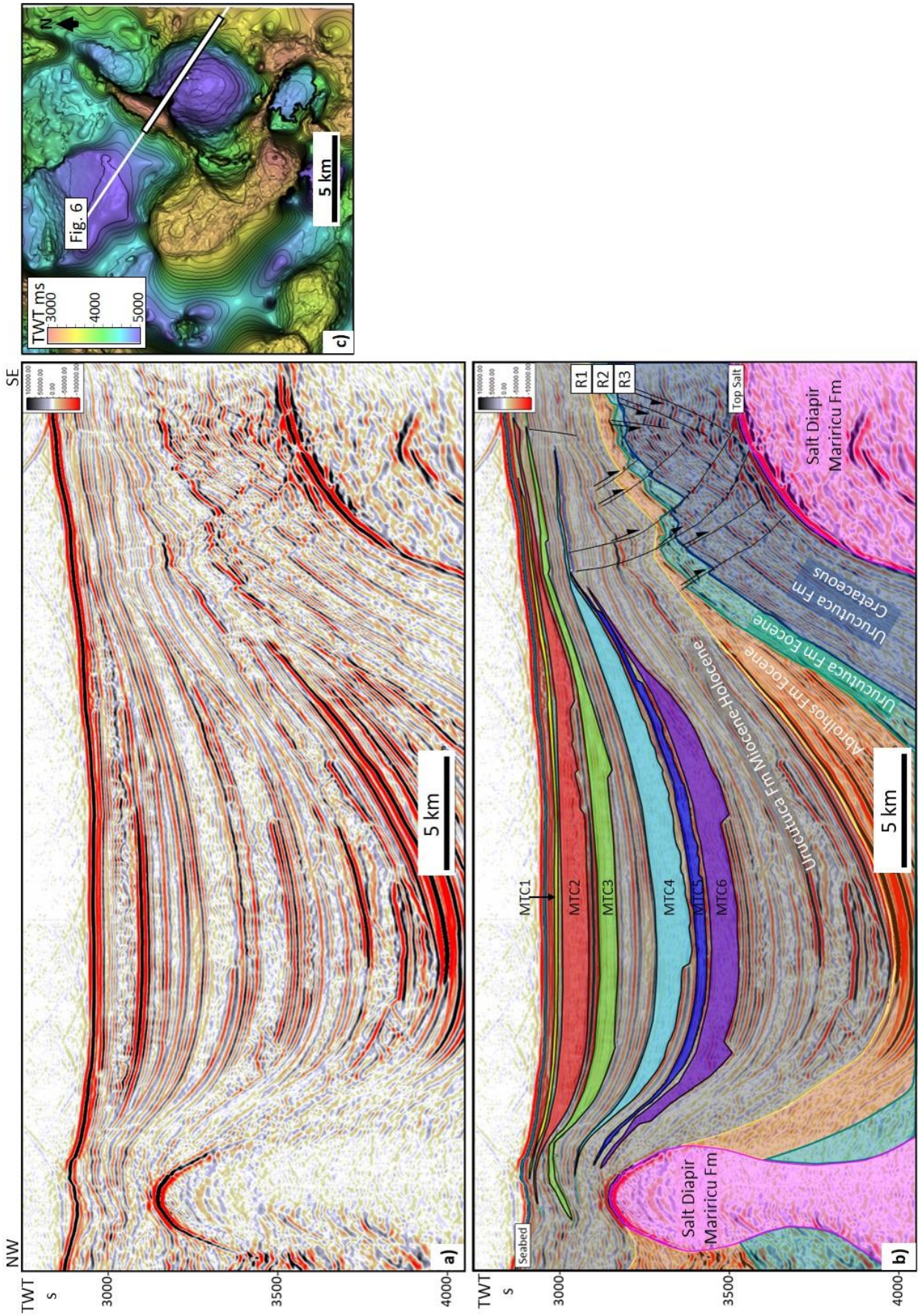
c)
TWT ms
3000
4000
5000
Fig. 6
N
5 km
SE
NW
TWT
s
3000
3500
4000
a)
5 km
b)
Seabed
MTC1
MTC2
MTC3
MTC4
MTC5
MTC6
R1
R2
R3
Top Salt
Salt Diapir
Mariricu Fm
Urucutuca Fm Miocene Holocene
Abrolhos Fm Eocene
Urucutuca Fm Eocene
Urucutuca Fm
Cretaceous
5 km

662 Figure 8

663

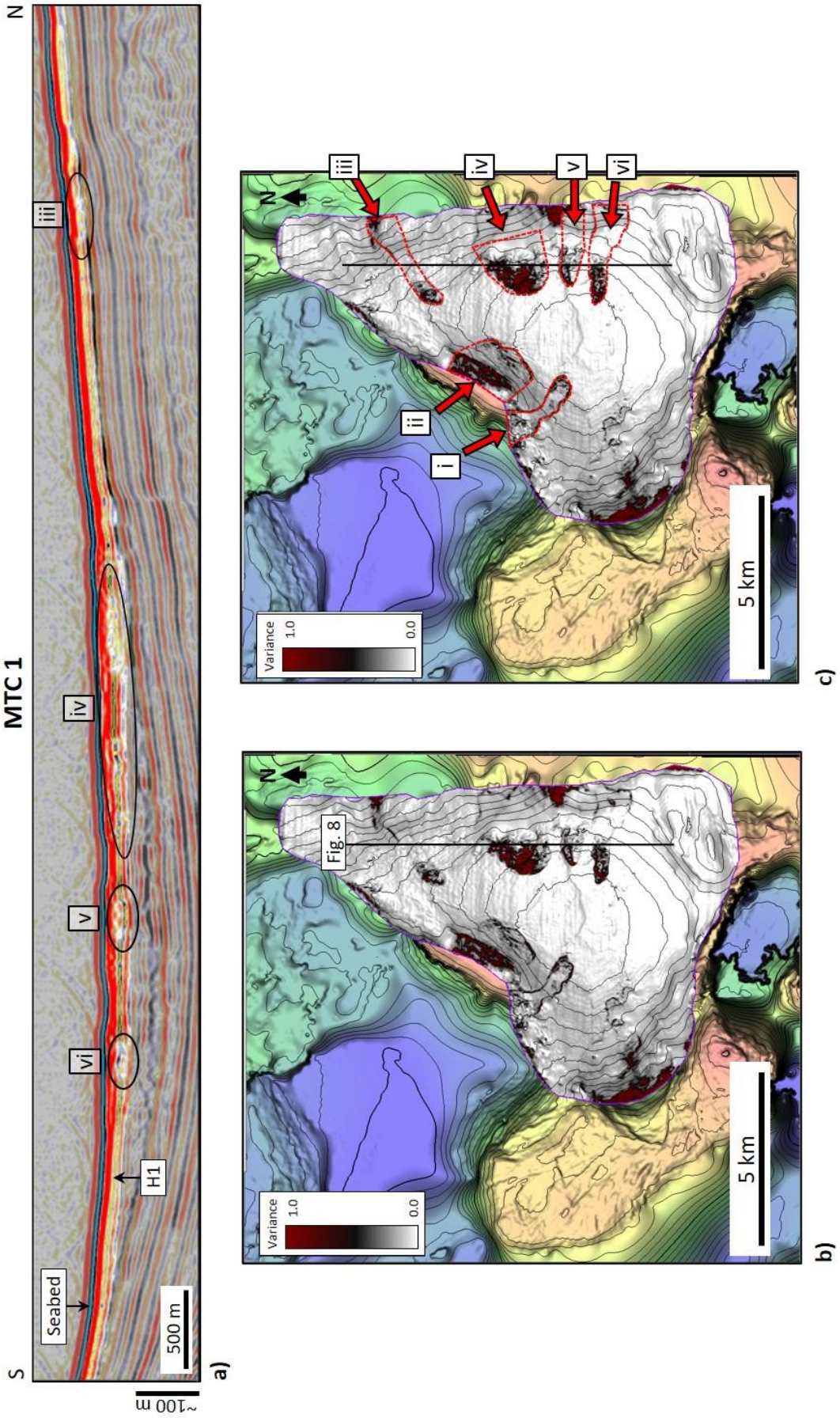

664 Figure 9

665

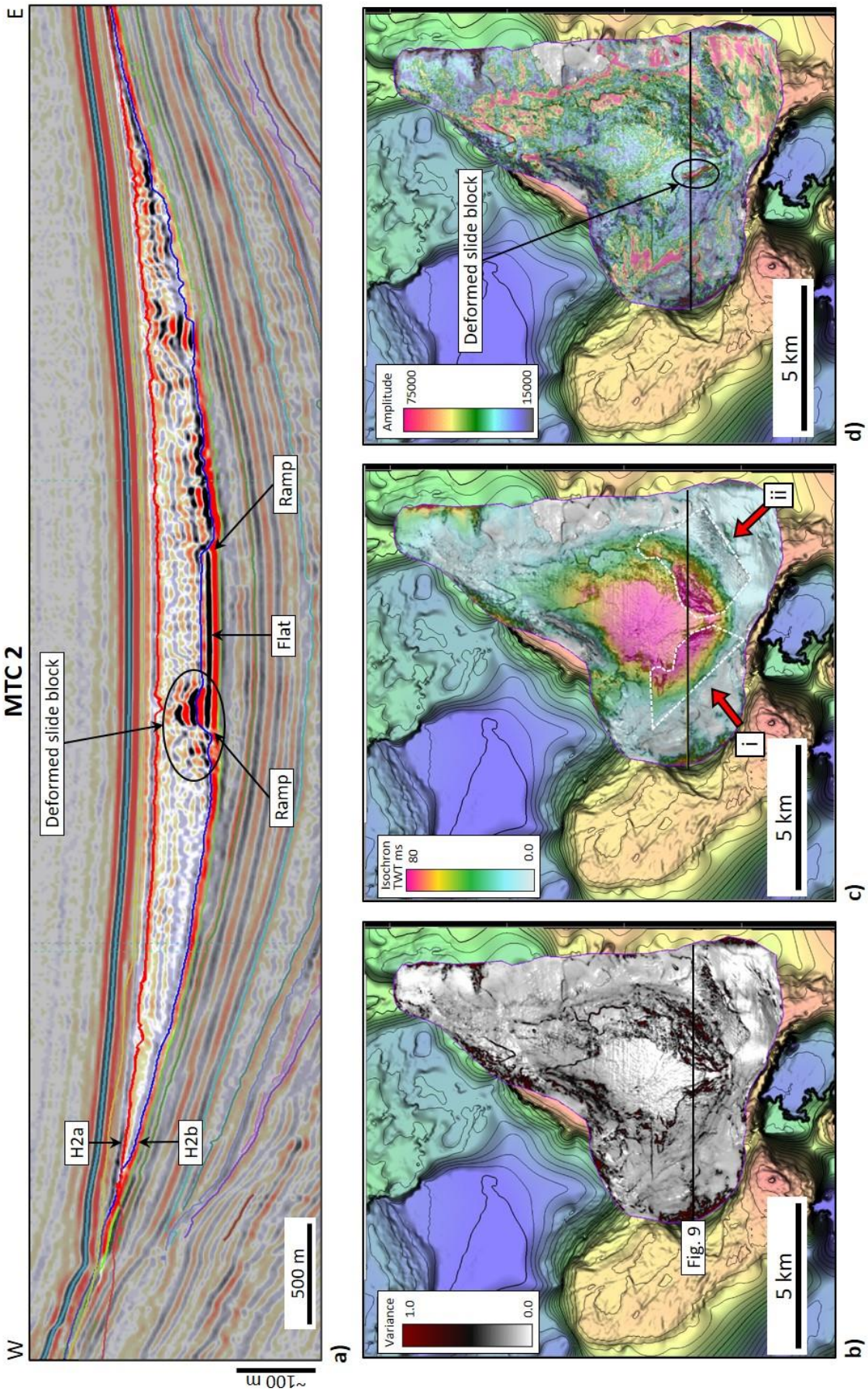

666 Figure 10

667

668

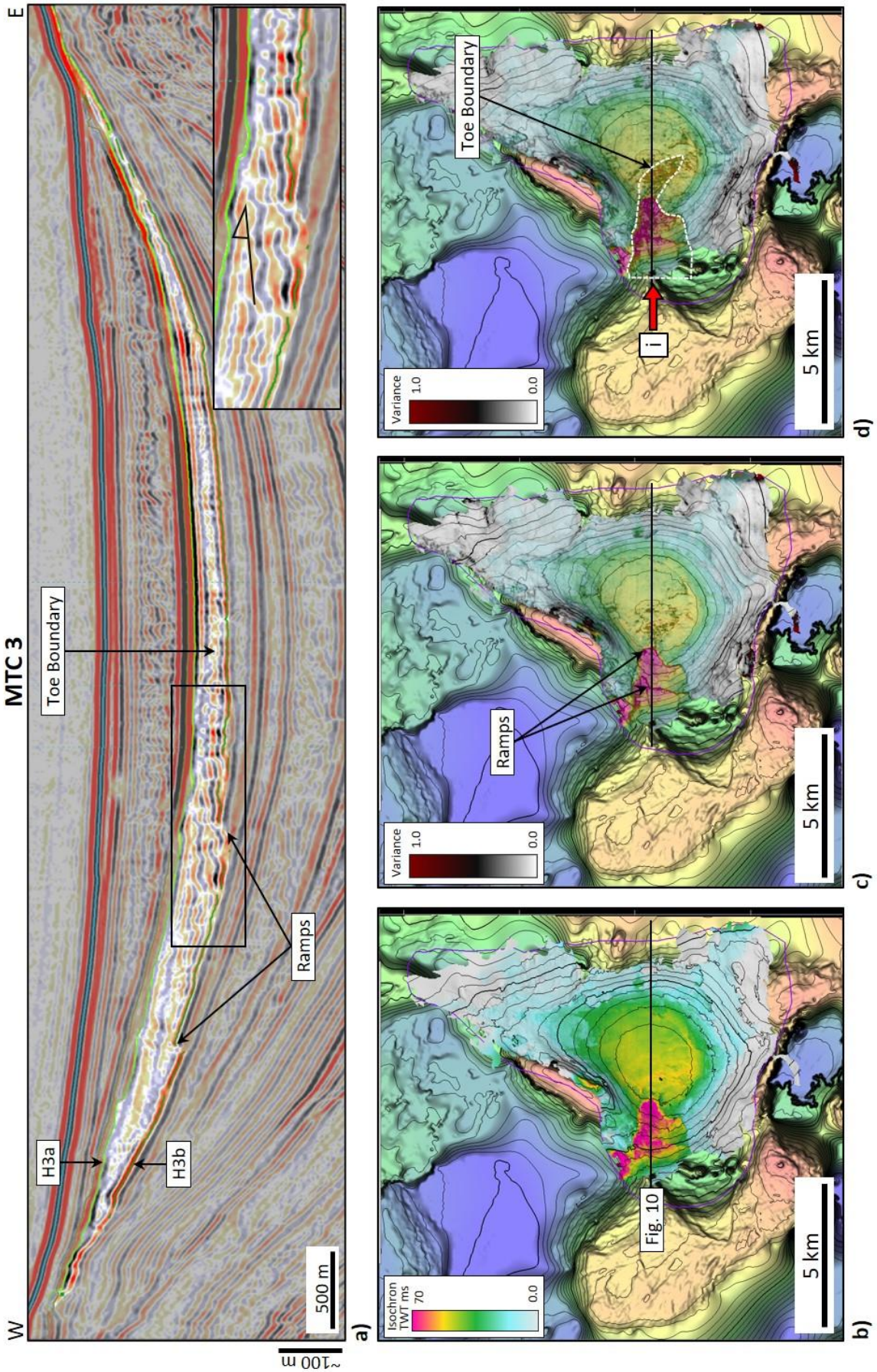

669 Figure 11

670

671

672

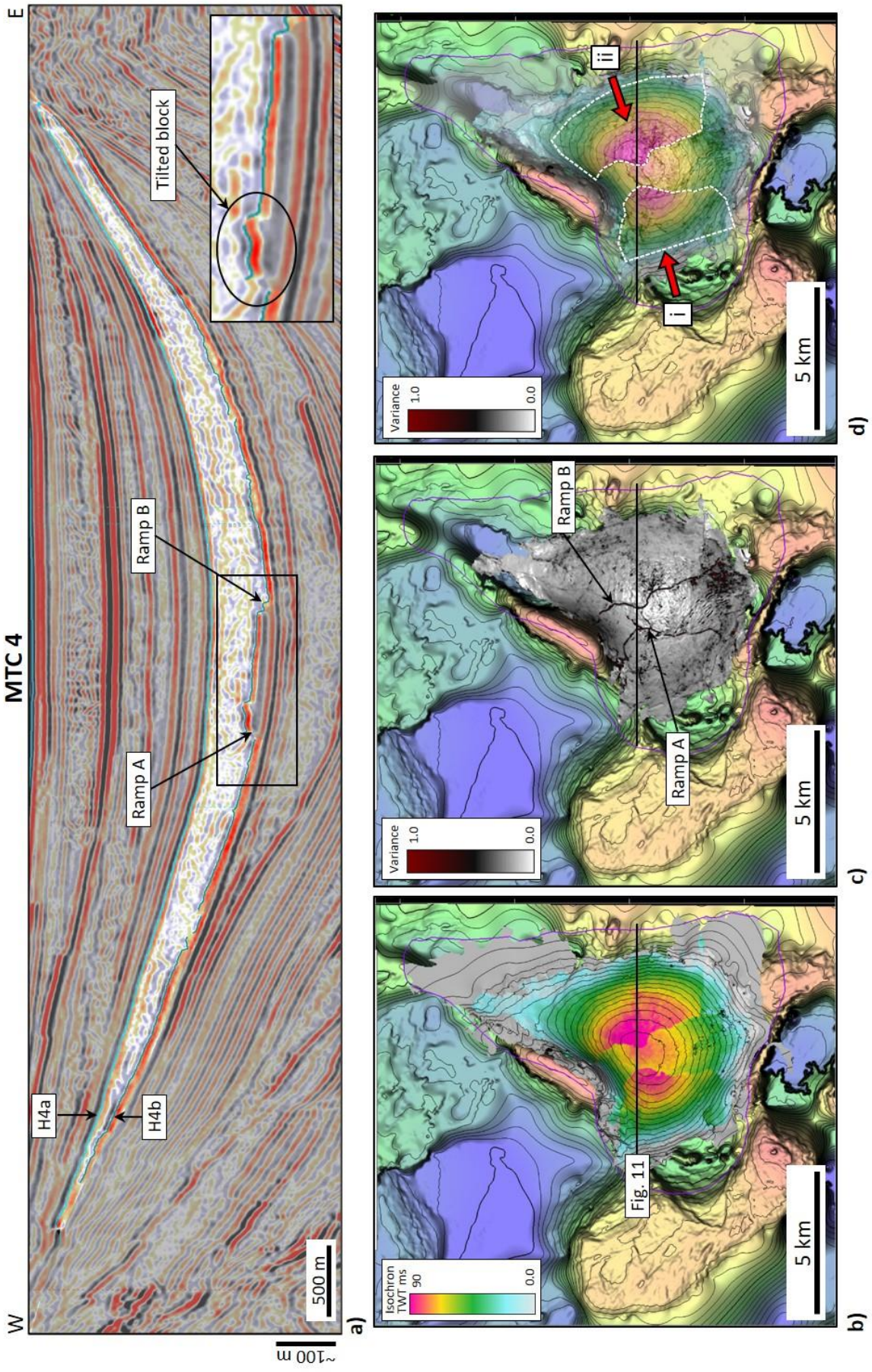

673 Figure 12

674

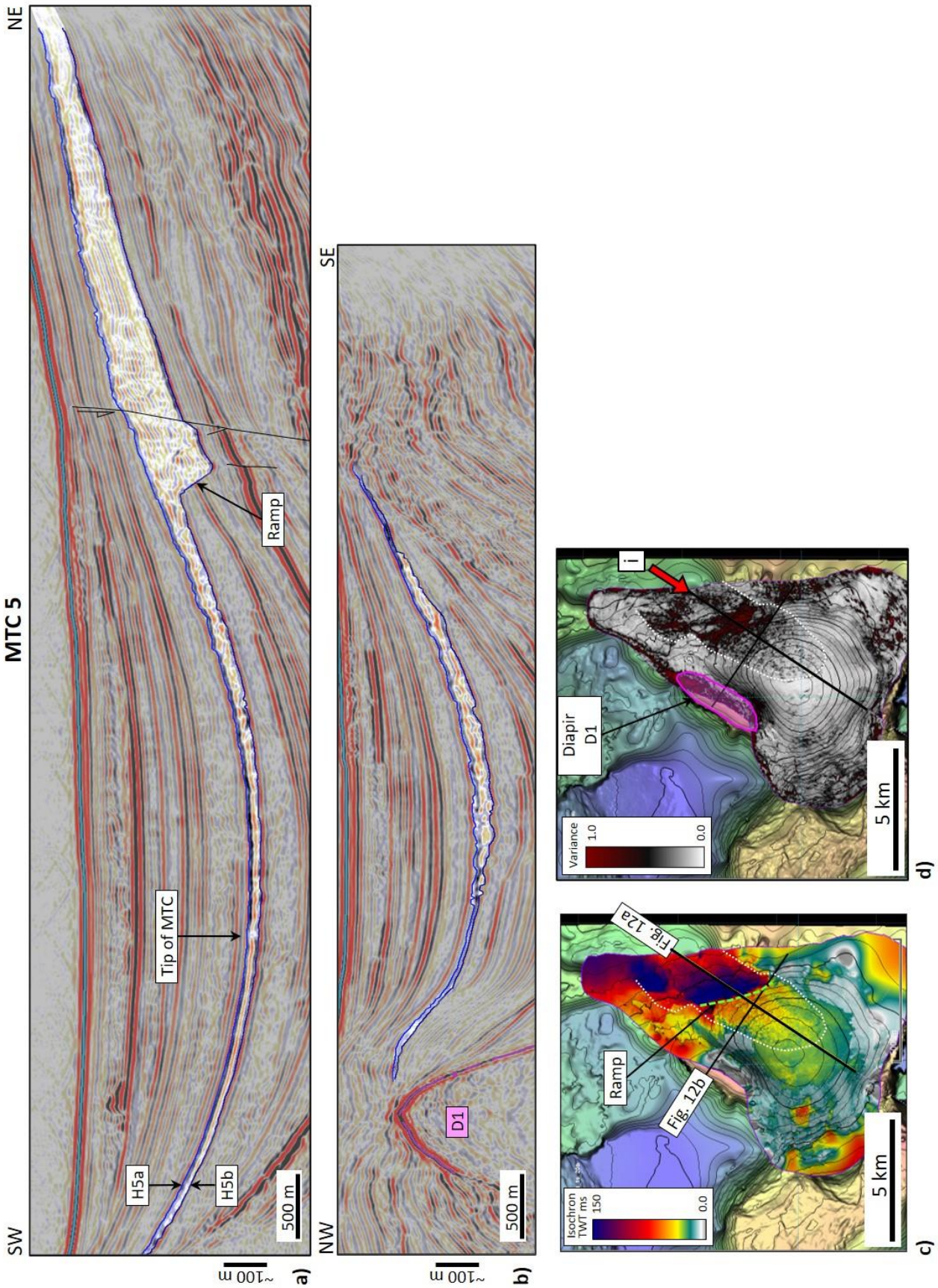

675 Figure 13

676

677

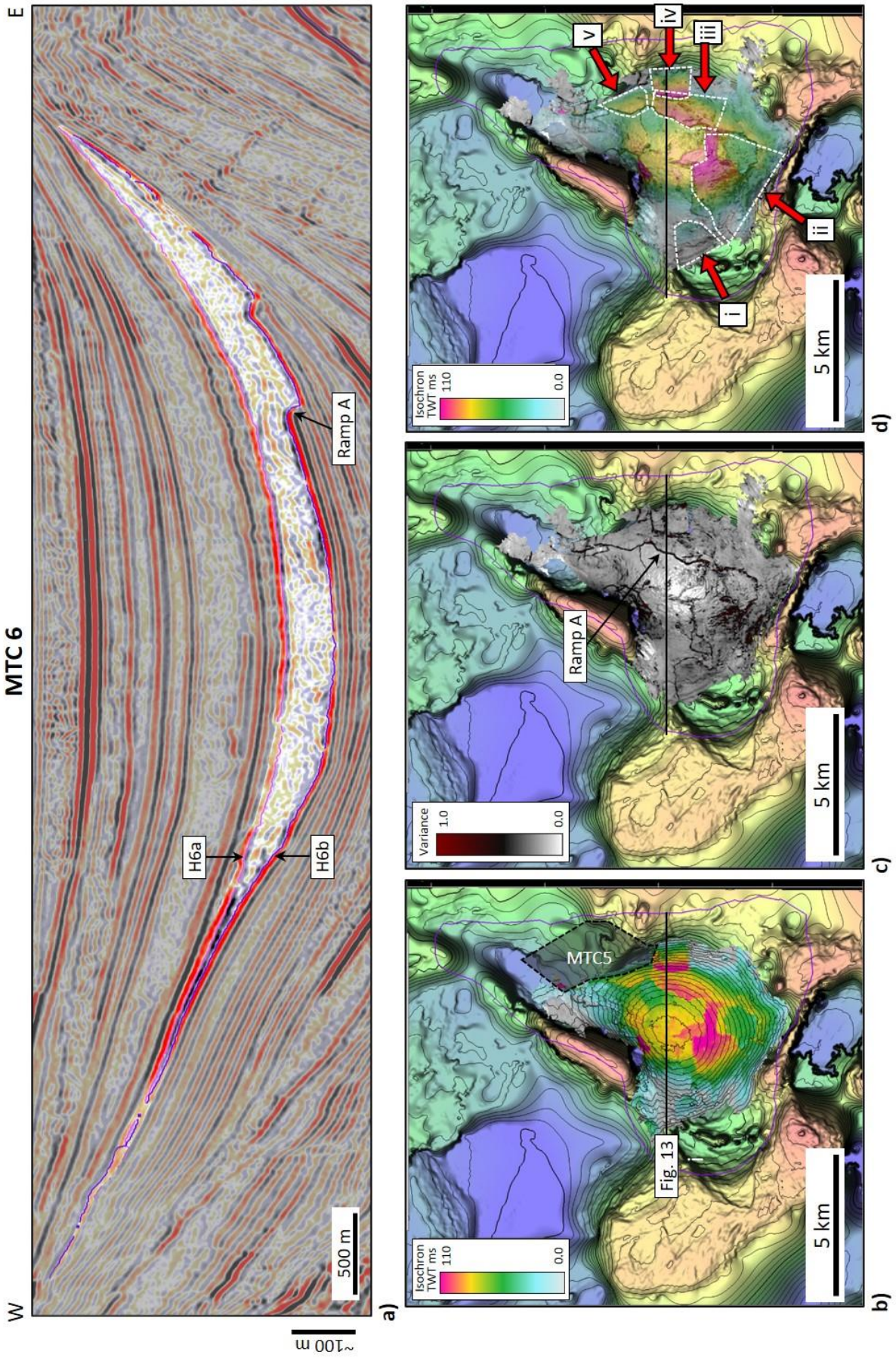

678 Figure 14

679

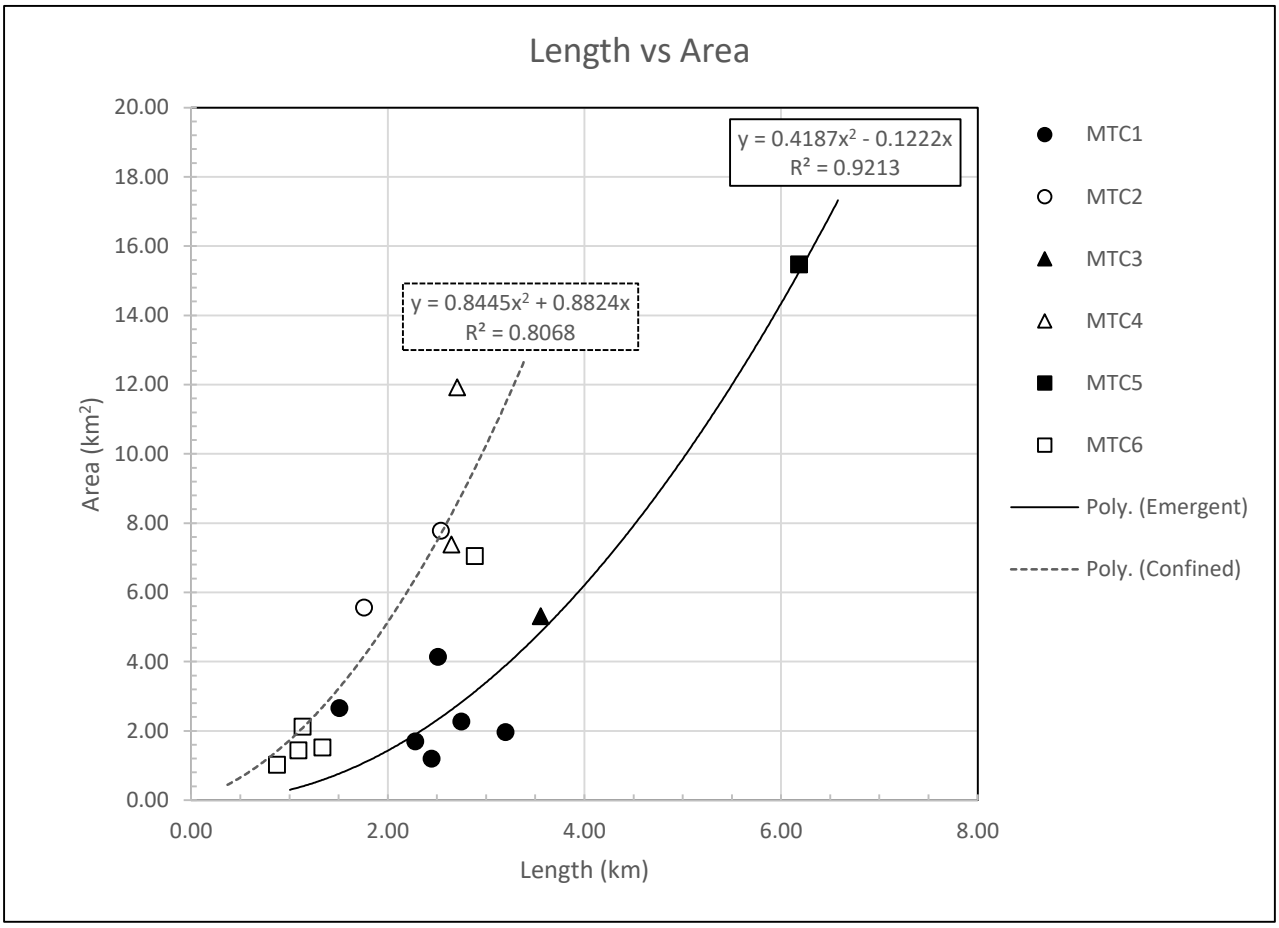

680

681 Figure 15

682

683

684

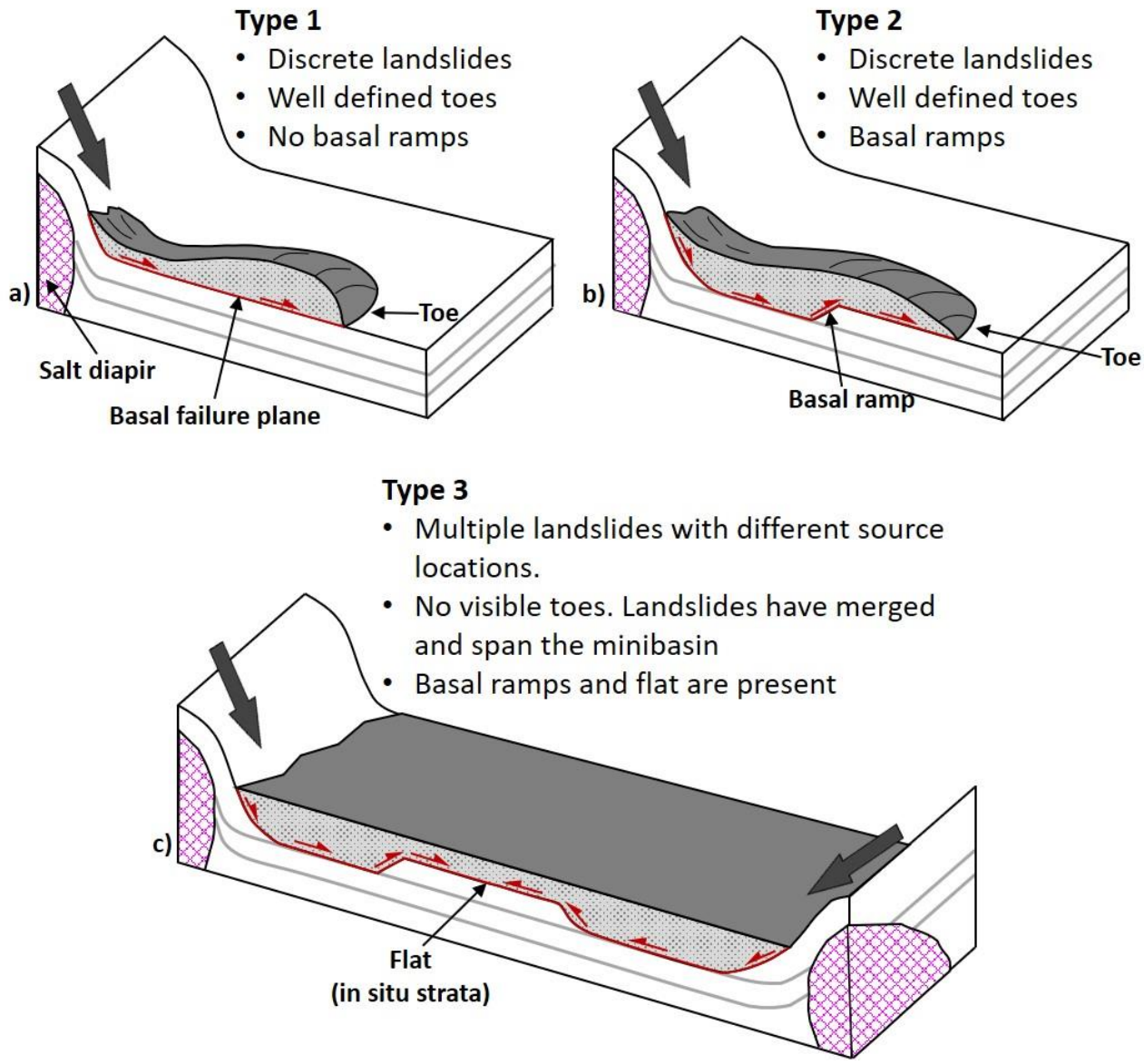

685 Figure 16

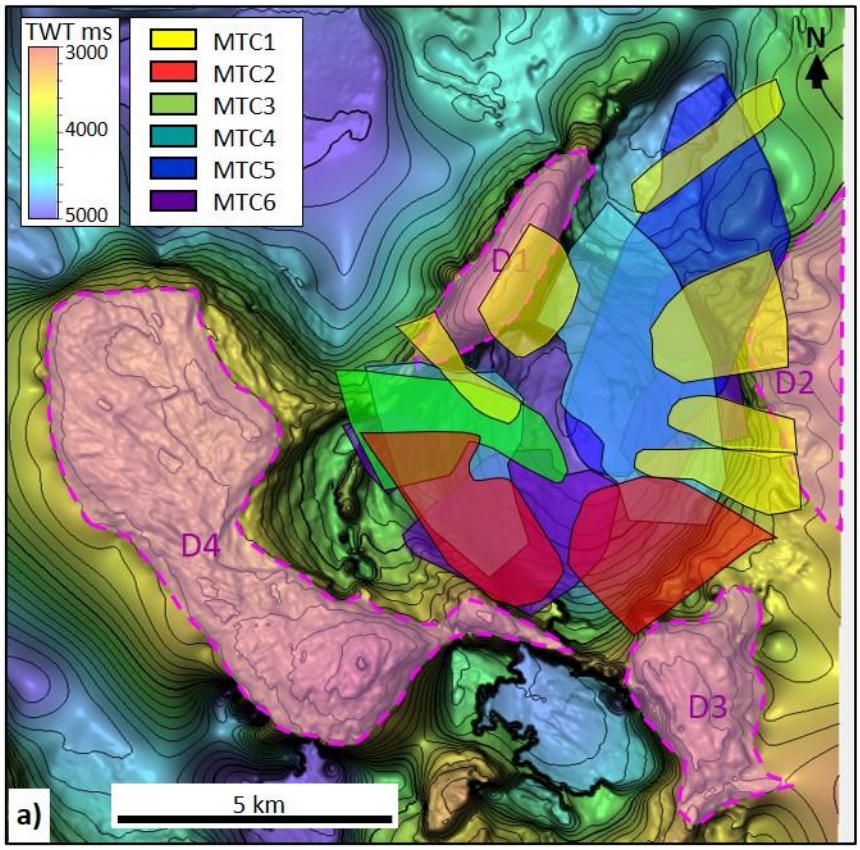

686

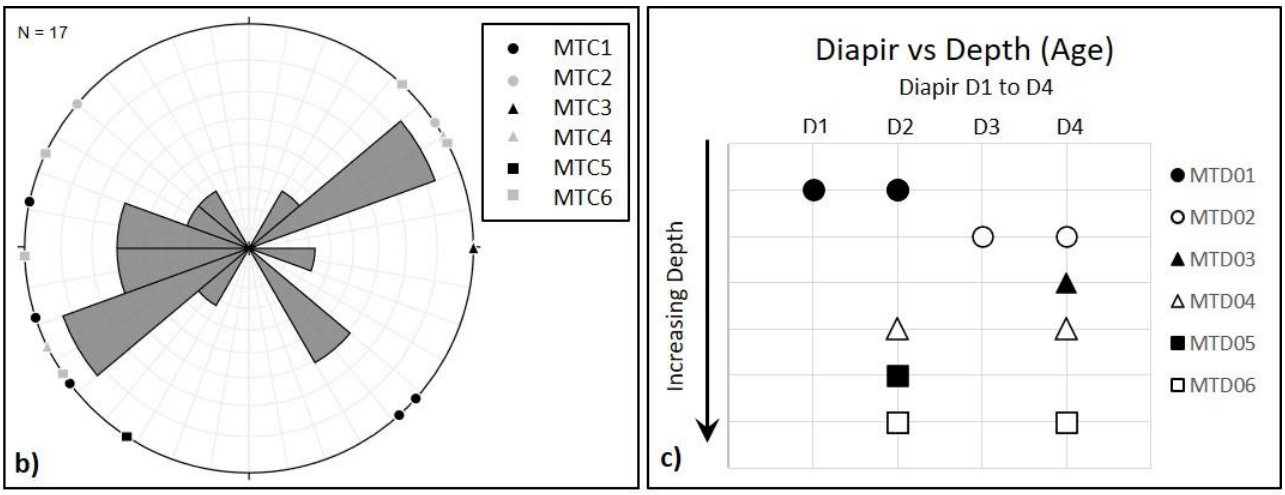

687

688

689

Tables

Table 1

MTC	Horizon	MTC Description	No of MTCs	Basal Ramps	Merged MTCs
MTC 1	H1	Six well defined MTCs with varied source directions and distinct edges including the toe. All MTCs appear on a single seismic reflector.	6	No	No
MTC 2	H2a H2b	Interpreted as 2 MTCs that have merged to span the basin. Basal ramps present, seismically opaque, except for high amplitude over-ramp emergence onto a central platform. Thickest in confined zones adjacent to ramps.	2	Yes	Yes
MTC 3	H3a H3b	Single MTC with a clearly defined toe. Multiple basal ramps, MTC is emergent onto the basin floor and is thickest near the source, in the confined zone. Internal structures are imaged on the seismic.	1	Yes	No
MTC 4	H4a H4b	Merged MTCs that fill the minibasin. No internal structure visible, two curved basal ramps bound a platform striking approximately N-S. MTC is thickest near the basin centre, adjacent to the ramps. The edge of the platform contains a tilted-block, deformed by the MTC.	2	Yes	Yes
MTC 5	H5a H5b	Single MTC with clearly boundaries and toe. MTC has one, large basal ramp, is emergent and is thickest near the source, in the confined zone. Internal structure is visible.	1	Yes	No
MTC 6	H6a H6b	Multiple MTCs with varied source directions that have merged to span the basin. MTCs have multiple basal ramps, thickest sections are adjacent to the ramps. Some internal structure is imaged on the seismic.	5	Yes	Yes
		Total	17		

695 Table 2

MTC	Individual MTC	Area km^2	Length km	Flow Direction ^{o} from N	Diapir (D1 to D4)
MTC 1	MTC1_i	**1.20**	2.4	132	1
	MTC1_ii	**2.66**	1.5	138	1
	MTC1_iii	**1.97**	3.2	233	
	MTC1_iv	**4.14**	2.5	252	2
	MTC1_v	**1.70**	2.3	282	2
	MTC1_vi	**2.27**	2.7	278	2
MTC 2	MTC2_i	7.78	2.5	310	4
	MTC2_ii	5.57	1.8	56	3
MTC 3	MTC3_i	**5.32**	3.6	90	4
MTC 4	MTC4_i	7.39	2.6	60	4
	MTC4_ii	11.93	2.7	244	2
MTC 5	MTC5_i	**15.47**	6.2	213	
MTC 6	MTC6_i	1.52	1.3	62	4
	MTC6_ii	7.05	2.9	43	4
	MTC6_iii	2.12	1.1	295	2
	MTC6_iv	1.44	1.1	268	2
	MTC6_v	1.02	0.9	236	2
Correlation for all Area to Length			0.74		
Correlation for emergent Area to Length			**0.92**		
Correlation for confined Area to Length			0.91		

696

697

698 Table 3

MTC	MTC Summary	MTC Type 1 to 3
MTC 1	Six discrete MTDs with defined toes. No basal ramps	1
MTC 2	Multiple MTCs, merged to span the minibasin. 2 MTDs are interpreted within the MTC. Basal ramps present.	3
MTC 3	One discrete MTD with defined toe. Basal ramps	2
MTC 4	Multiple MTCs, merged to span the minibasin. 2 MTDs are interpreted within the MTC. Basal ramps present.	3
MTC 5	One discrete MTD with defined toe. Basal ramps	2
MTC 6	Multiple MTCs, merged to span the minibasin. 5 MTDs are interpreted within the MTC. Basal ramps present.	3

699

700

Acknowledgements

The authors would like to acknowledge CGG for providing the 3D seismic volume and allowing images of the data to be shown. We thank Schlumberger for granting Petrel academic licences to Cardiff's 3D Seismic Lab. The authors acknowledge the Brazilian National Petroleum Agency (ANP) for the well data provided. The authors would like to thank Nathalia Mattos and the reviewers for their constructive comments. This research did not receive any specific grant from funding agencies in the public, commercial, or not-for-profit sectors.

References

Alves, T.M., 2015. Submarine slide blocks and associated soft-sediment deformation in deep-water basins: A review. Mar. Pet. Geol. 67, 262–285. https://doi.org/10.1016/j.marpetgeo.2015.05.010

Alves, T.M., Fetter, M., Lima, C., Cartwright, J.A., Cosgrove, J., Gangá, A., Queiroz, C.L., Strugale, M., 2017. An incomplete correlation between pre-salt topography, top reservoir erosion, and salt deformation in deep-water Santos Basin (SE Brazil). Mar. Pet. Geol. 79, 300–320. https://doi.org/10.1016/j.marpetgeo.2016.10.015

Alves, T.M., Lourenço, S.D.N., 2010. Geomorphologic features related to gravitational collapse: Submarine landsliding to lateral spreading on a Late Miocene-Quaternary slope (SE Crete, eastern Mediterranean). Geomorphology 123, 13–33. https://doi.org/10.1016/j.geomorph.2010.04.030

Assumpção, M., Dourado, J.C., Ribotta, L.C., Mohriak, W.U., Dias, F.L., Barbosa, J.R., 2011. The São Vicente earthquake of 2008 April and seismicity in the continental shelf off SE Brazil: Further evidence for flexural stresses. Geophys. J. Int. 187, 1076–1088. https://doi.org/10.1111/j.1365-246X.2011.05198.x

Baeten, N.J., Laberg, J.S., Forwick, M., Vorren, T.O., Vanneste, M., Forsberg, C.F., Kvalstad, T.J.,

724 Ivanov, M., 2013. Morphology and origin of smaller-scale mass movements on the continental
725 slope off northern Norway. Geomorphology 187, 122–134.
726 https://doi.org/10.1016/j.geomorph.2013.01.008

727 Beaubouef, R.T., Abreu, V., 2010. MTCs of the Brazos-Trinity slope system; thoughts on the
728 sequence stratigraphy of MTCs and their possible roles in shaping hydrocarbon traps, in:
729 Submarine Mass Movements and Their Consequences. Springer, pp. 475–490.

730 Calvès, G., Huuse, M., Clift, P.D., Brusset, S., 2015. Giant fossil mass wasting off the coast of West
731 India: The Nataraja submarine slide. Earth Planet. Sci. Lett. 432, 265–272.
732 https://doi.org/10.1016/j.epsl.2015.10.022

733 Canals, M., Lastras, G., Urgeles, R., Casamor, J.L., Mienert, J., Cattaneo, A., Batist, M. De,
734 Haflidason, H., Imbo, Y., Laberg, J.S., Locat, J., Long, D., Longva, O., Masson, D.G., Sultan,
735 N., Trincardi, F., Bryn, P., 2004. Slope failure dynamics and impacts from seafloor and shallow
736 sub-seafloor geophysical data: case studies from the COSTA project. Mar. Geol. 213, 9–72.
737 https://doi.org/https://doi.org/10.1016/j.margeo.2004.10.001

738 Cardona, S., Wood, L.J., Day-Stirrat, R.J., Moscardelli, L., 2016. Fabric development and pore-throat
739 reduction in a mass-transport deposit in the Jubilee Gas Field, Eastern Gulf of Mexico:
740 consequences for the sealing capacity of MTDs, in: Submarine Mass Movements and Their
741 Consequences. Springer, pp. 27–37.

742 Chang, H.K., Kowsmann, R.O., Figueiredo, A.M.F., Bender, A., 1992. Tectonics and stratigraphy of
743 the East Brazil Rift system: an overview. Tectonophysics 213, 97–138.
744 https://doi.org/10.1016/0040-1951(92)90253-3

745 Clare, M., Chaytor, J., Dabson, O., Gamboa, D., Georgiopoulou, A., Eady, H., Hunt, J., Jackson, C.,
746 Katz, O., Krastel, S., León, R., Micallef, A., Moernaut, J., Moriconi, R., Moscardelli, L.,

747 Mueller, C., Normandeau, A., Patacci, M., Steventon, M., Urlaub, M., Völker, D., Wood, L.,
748 Jobe, Z., 2018. A consistent global approach for the morphometric characterization of
749 subaqueous landslides. Geol. Soc. London, Spec. Publ. SP477.15.
750 https://doi.org/10.1144/sp477.15

751 Crandell, D.R., Miller, C.D., Glicken, H.X., Christiansen, R.L., Newhall, C.G., 1984. Catastrophic
752 debris avalanche from ancestral Mount Shasta volcano, California. Geology 12, 143–146.
753 https://doi.org/10.1130/0091-7613(1984)12<143:CDAFAM>2.0.CO;2

754 Davison, I., 2007. Geology and tectonics of the South Atlantic Brazilian salt basins. Geol. Soc.
755 London, Spec. Publ. 272, 345–359. https://doi.org/10.1144/GSL.SP.2007.272.01.18

756 Doughty-Jones, G., Lonergan, L., Mayall, M., Dee, S.J., 2019. The role of structural growth in
757 controlling the facies and distribution of mass transport deposits in a deep-water salt minibasin.
758 Mar. Pet. Geol. 104, 106–124. https://doi.org/10.1016/j.marpetgeo.2019.03.015

759 Fiduk, J.C., Brush, E.R., Anderson, L.E., Gibbs, P.B., Rowan, M.G., 2004. Salt Deformation,
760 Magmatism, and Hydrocarbon Prospectivity in the Espirito Santo Basin, Offshore Brazil.

761 França, R.L., Del Rey, A.C., Tagliari, C.V., Brandão, J.R., De Rossi Fontanelli, P., 2007. Bacia do
762 Espírito Santo. Bol. Geociencias da Petrobras 15, 501–509.

763 Frey-Martínez, J., Cartwright, J., James, D., 2006. Frontally confined versus frontally emergent
764 submarine landslides: A 3D seismic characterisation. Mar. Pet. Geol. 23, 585–604.
765 https://doi.org/https://doi.org/10.1016/j.marpetgeo.2006.04.002

766 Gamboa, D., Alves, T.M., 2016. Bi-modal deformation styles in confined mass-transport deposits:
767 Examples from a salt minibasin in SE Brazil. Mar. Geol. 379, 176–193.
768 https://doi.org/https://doi.org/10.1016/j.margeo.2016.06.003

769 Gamboa, D., Alves, T.M., Cartwright, J., Terrinha, P., 2010. MTD distribution on a ‘passive’

continental margin: The Espírito Santo Basin (SE Brazil) during the Palaeogene. Mar. Pet. Geol. 27, 1311–1324. https://doi.org/https://doi.org/10.1016/j.marpetgeo.2010.05.008

Gamboa, D., Alves, T.M., Omosanya, K.O., 2019. Style and Morphometry of Mass-Transport Deposits Across the Espírito Santo Basin (Offshore SE Brazil), in: Submarine Landslides. American Geophysical Union (AGU), pp. 227–246. https://doi.org/10.1002/9781119500513.ch14

Gee, M.J.R., Gawthorpe, R.L., Friedmann, S.J., 2006. Triggering and Evolution of a Giant Submarine Landslide, Offshore Angola, Revealed by 3D Seismic Stratigraphy and Geomorphology. J. Sediment. Res. 76, 9–19. https://doi.org/10.2110/jsr.2006.02

Georgiopoulou, A., Benetti, S., Shannon, P.M., Sacchetti, F., Haughton, P.D.W., Comas-Bru, L., Krastel, S., 2014. Comparison of mass wasting processes on the slopes of the Rockall Trough, Northeast Atlantic, in: Submarine Mass Movements and Their Consequences. Springer, pp. 471–480.

Gibbs, P.B., Brush, E.R., Fiduk, J.C., 2003. The evolution of the syn-rift and transition phases of the central / southern Brazilian and W. African conjugate margins: the implications for source rock distribution in time and space, and their recognition on seismic data. 8th Congr. Int. Soc. Bras. Geofis. 1–6.

Giles, K.A., Lawton, T.F., 2002. Halokinetic sequence stratigraphy adjacent to the El Papalote diapir, Northeastern Mexico. Am. Assoc. Pet. Geol. Bull. 86, 823–840. https://doi.org/10.1306/61eedbac-173e-11d7-8645000102c1865d

Giles, K.A., Rowan, M.G., 2012. Concepts in halokinetic-sequence deformation and stratigraphy. Geol. Soc. London, Spec. Publ. 363, 7 LP – 31.

Haflidason, H., Lien, R., Sejrup, H.P., Forsberg, C.F., Bryn, P., 2005. The dating and morphometry

of the Storegga Slide. Mar. Pet. Geol. 22, 123–136. https://doi.org/10.1016/J.MARPETGEO.2004.10.008

Hampton, M.A., Lee, H.J., Locat, J., 1996. Submarine landslides. Rev. Geophys. 34, 33–59. https://doi.org/10.1029/95RG03287

Henry, L.C., Wadsworth, J.A., Hansen, B., Hartman, K., 2018. Erosion and ponding of Thunder Horse deepwater turbidites by mass transport complexes in Mississippi Canyon based on image log sedimentology. Mar. Pet. Geol. 97, 639–658. https://doi.org/10.1016/j.marpetgeo.2018.08.006

Jackson, C.A.-L., 2012. The initiation of submarine slope failure and the emplacement of mass transport complexes in salt-related minibasins: A three-dimensional seismic-reflection case study from the Santos Basin, offshore Brazil. Bulletin 124, 746–761.

Johnson, H.P., Helferty, M., 1990. Side-Scan Interpretation of Sonar. Rev. Geophys. 28, 357–380.

Katz, O., Reuven, E., Aharonov, E., 2015. Submarine landslides and fault scarps along the eastern Mediterranean Israeli continental-slope. Mar. Geol. 369, 100–115. https://doi.org/10.1016/j.margeo.2015.08.006

Lackey, J., Moore, G., Strasser, M., 2018. Three-dimensional mapping and kinematic characterization of mass transport deposits along the outer Kumano Basin and Nankai accretionary wedge, southwest Japan. Prog. Earth Planet. Sci. 5. https://doi.org/10.1186/s40645-018-0223-4

Locat, J., Lee, H.J., 2002. Submarine landslides: advances and challenges. Can. Geotech. J. 39, 193–212.

McAdoo, B.G., Pratson, L.F., Orange, D.L., 2000. Submarine landslide geomorphology, US continental slope. Mar. Geol. 169, 103–136. https://doi.org/10.1016/S0025-3227(00)00050-5

816 Mianaekere, V., Adam, J., 2020. 'Halo-kinematic' sequence stratigraphic analysis adjacent to salt
817 diapirs in the deepwater contractional province, Liguro-Provençal Basin, Western
818 Mediterranean Sea. Mar. Pet. Geol. 115, 104258.
819 https://doi.org/10.1016/j.marpetgeo.2020.104258

820 Mohriak, W., Nemčok, M., Enciso, G., 2008. South Atlantic divergent margin evolution: rift-border
821 uplift and salt tectonics in the basins of SE Brazil. Geol. Soc. London, Spec. Publ. 294, 365–
822 398. https://doi.org/10.1144/SP294.19

823 Moscardelli, L., Wood, L., 2016. Morphometry of mass-transport deposits as a predictive tool. GSA
824 Bull. 47–80. https://doi.org/https://doi.org/10.1130/B31221.1

825 Moscardelli, L., Wood, L., 2008. New classification system for mass transport complexes in offshore
826 Trinidad. Basin Res. 20, 73–98. https://doi.org/10.1111/j.1365-2117.2007.00340.x

827 Moscardelli, L., Wood, L., Mann, P., 2006. Mass-transport complexes and associated processes in
828 the offshore area of Trinidad and Venezuela. Am. Assoc. Pet. Geol. Bull. 1059–1088.
829 https://doi.org/https://doi.org/10.1306/02210605052

830 Mulder, T ; Cochonat, P., 1996. Classification of offshore mass movements. J. Sediment. Res. 66(1),
831 43–57.

832 Ojeda, H.A.O., 1982. Structural framework, stratigraphy, and evolution of Brazilian marginal basins.
833 Am. Assoc. Pet. Geol. Bull. 66, 732–749.

834 Omosanya, K.O., Alves, T.M., 2013. A 3-dimensional seismic method to assess the provenance of
835 Mass-Transport Deposits (MTDs) on salt-rich continental slopes (Espírito Santo Basin, SE
836 Brazil). Mar. Pet. Geol. 44, 223–239. https://doi.org/10.1016/j.marpetgeo.2013.02.006

837 Pickering, K.T., Corregidor, J., 2005. Mass-Transport Complexes (MTCs) and Tectonic Control on
838 Basin-Floor Submarine Fans, Middle Eocene, South Spanish Pyrenees. J. Sediment. Res. 75,

761–783. https://doi.org/10.2110/jsr.2005.062

Ponte, F.C., Asmus, H.E., 1978. Geological framework of the Brazilian continental margin. Geol. Rundschau 67, 201–235.

Schulten, I., Mosher, D.C., Piper, D.J.W., Krastel, S., 2019. A Massive Slump on the St. Pierre Slope, A New Perspective on the 1929 Grand Banks Submarine Landslide. J. Geophys. Res. Solid Earth 124, 7538–7561. https://doi.org/10.1029/2018JB017066

Schuster, R.L., Highland, L.M., 2001. Socioeconomic Impacts of Landslides in the Western Hemisphere. U.S. Geol. Surv. Open-File Rep. 01-276 Open-File.

Shanmugam, G., Shrivastava, S.K., Das, B., 2009. Sandy Debrites and Tidalites of Pliocene Reservoir Sands in Upper-Slope Canyon Environments, Offshore Krishna-Godavari Basin (India): Implications. J. Sediment. Res. 79, 736–756. https://doi.org/10.2110/jsr.2009.076

Tripsanas, E.K., Bryant, W.R., Phaneuf, B.A., 2004. Slope-instability processes caused by salt movements in a complex deep-water environment, Bryant Canyon area, northwest Gulf of Mexico. Am. Assoc. Pet. Geol. Bull. 88, 801–823.

Van Bemmel, P.P., Pepper, R.E.F., 2000. Seismic signal processing method and apparatus for generating a cube of variance values.

Varnes, D.J., 1978. Slope movement types and processes. Spec. Rep. 176.

Völker, D., Geersen, J., Behrmann, J.H., Weinrebe, W.R., 2012. Submarine mass wasting off Southern Central Chile: distribution and possible mechanisms of slope failure at an active continental margin, in: Submarine Mass Movements and Their Consequences. Springer, pp. 379–389.

Ward, N.I.P., Alves, T.M., Blenkinsop, T.G., 2018. Submarine sediment routing over a blocky mass-transport deposit in the Esprito Santo Basin, SE Brazil. Basin Res. 30, 816–834.

862 Weimer, P., Shipp, C., 2004. Mass transport complex: Musing on past uses and suggestions for future
863 directions. Proc. Annu. Offshore Technol. Conf. 3, 2012–2021. https://doi.org/10.4043/16752-
864 ms

865 Wu, N., Jackson, C.A.L., Johnson, H.D., Hodgson, D.M., Nugraha, H.D., 2020. Mass-transport
866 complexes (MTCs) document subsidence patterns in a northern Gulf of Mexico salt minibasin.
867 Basin Res. 1–28. https://doi.org/10.1111/bre.12429

868 Yamamoto, Y., Chiyonobu, S., Kanamatsu, T., Ahagon, N., Aoike, K., Kamiya, N., Ojima, T., Hirose,
869 T., Sugihara, T., Saito, S., Kinoshita, M., Kubo, Y., Yamada, Y., 2019. Repeated large-scale
870 mass-transport deposits and consequent rapid sedimentation in the western part of the Bay of
871 Bengal, India. Geol. Soc. London, Spec. Publ. 477, 183–193. https://doi.org/10.1144/sp477.12